THE ORIGIN OF STRUCTURE AND TURBULENCE IN GALACTIC DISKS

THE ORIGIN OF STRUCTURE AND TURBULENCE IN GALACTIC DISKS

By

COLIN MCNALLY, B.Sc.

A Thesis
Submitted to the School of Graduate Studies
in Partial Fulfillment of the Requirements
for the Degree
Master of Science

McMaster University

MASTER OF SCIENCE (2007) McMaster University
(Physics) Hamilton, Ontario

TITLE: The Origin of Structure and Turbulence in Galactic Disks

AUTHOR: Colin M^{c}Nally, B.Sc.(McGill)

SUPERVISOR: Dr. H. M. P. Couchman & Dr. J. Wadsley

NUMBER OF PAGES: xiii, 83

Abstract

Through HI observations, galactic gas discs can be observed to extend past the edge of the star forming disk. Observations of HI in these extended galactic disks consistently show significant velocity dispersion, which suggests a non-thermal origin. This suggests that turbulence in the gas is contributing significantly to the observed velocity dispersion. To address this, a new parallel adaptive mesh three dimensional shearing-box implementation with adaptions for evening numerical diffusion effects, self-gravity in the shearing boundary conditions and appropriate vertical boundary conditions has been built, based on the FLASH code. This code is used to perform local simulations, incorporating differential rotation, self-gravity, stratification, hydrodynamics and cooling. These simulations explore possible mechanisms for driving turbulent motions through thermal and self-gravitational instabilities coupling to differential rotation. In isothermal simulations a marginally stable disk is found to be stable against forming a gravitoturbulent quasi-steady state. In simulations including cooling, where the disk conditions do not trigger the formation of a two-phase medium, it is found that perturbations to the flow damp without leading to a sustained mechanism for driving turbulence. In cases where a two-phase medium develops, gravitational angular momentum transporting stresses are much greater, creating a possible mechanism for transferring energy from galactic rotation to turbulence, though a gravitoturbulent quasi-steady state is not found. The differing angular momentum transport properties of the single phase and two phase regimes of the disk suggests a significant dynamical division can be drawn between the two, which may occur far outside the star formation cutoff in a galactic disk.

Acknowledgements

My advisers, Hugh Couchman and James Wadsley, have taught, advised, financially supported and tolerated me not only during the 2 years of my M.Sc., but for 5 years before that. Without this continuous support, I would not be doing astrophysics today.

The software used in this work was in part developed by the DOE-supported ASE / Alliance Center for Astrophysical Thermonuclear Flashes at the University of Chicago.

This work was made possible by the facilities of the Shared Hierarchical Academic Research Computing Network (SHARCNET:`www.sharcnet.ca`), and the staff that maintain those facilities.

Contents

List of Figures

List of Tables

Chapter 1

Introduction

Galaxies, though identifiable to the eye as a collection of stars, are complex systems dominated by dark matter and with significant components of gas and dust. The significance of these latter two baryonic components is that they provide the material from which the stellar component is formed. At least in the case of disk galaxies, in the later stages of galactic evolution, the baryonic components follow the gravitational influence of the dark matter, but the baryonic components only have a small effect on the form of the dark matter halo. The evolution of the stellar and gaseous components of the galaxy are, however, connected by their influences on each other. When sufficiently cool and dense concentrations form in the gas component, stars form and this in turn heats the gas and stirs up turbulent motions (see for example Freeman and Bland-Hawthorn, 2002). Though intimately connected to star formation, the gas component of disk galaxies sometimes continues far outside the extent of the stellar disk. This extended part of the gas disk is observed in HI emission to have significant small-scale motions. However, this region of such a galaxy is largely devoid of stars. This leads to a puzzle: how do the motions originate and what, dynamically, is happening to the gas disk?

To build an understanding of these questions, it is important to under-

stand the action of some basic processes in galactic gas disks. It is hoped that this will provide some understanding of the factors influencing the evolution of a galactic gas disk and provide insights into their observed properties.

1.0.1 Basic Observational Parameters

Observations of HI velocity dispersion curves show significant consistency between galaxies. Since these velocity dispersions are inferred by HI emission line width, they are velocity dispersions in the line of sight. After removing orbital motion, only vertical (e.g. face on) velocity dispersions can be inferred. Vertical velocity dispersions vary from $12 - 15$ km s^{-1} in central regions to $6 - 8$ km s^{-1} in outer regions, exceeding in many cases that expected from thermal broadening in the outer regions (Dib et al., 2006). By way of examples, published curves for ESO 215-G?009[1] and NGC 1058 in are reproduced in figure (1.1) and in figure (1.2) respectively. For ESO 215-G?009, Warren et al. (2004) find a disk of approximately constant HI surface density $7.25 M_{\odot}$ pc^{-2} from $100'' - 300''$. Levine et al. (2006a) show surface density maps of HI gas in the Milky Way, which are useful to determine the range of surface densities to consider – these are on the order of only a few $M_{\odot}$ pc^{-2}. From the same survey data, Levine et al. (2006b) give a vertical half-height map of HI in the outer Milky Way, one can consider values in the range of $500 - 4000$ pc to be reasonable as an ballpark half-height. Additionally, de Blok and Walter (2006) show a detection of two-component warm/cool HI in outer non-star-forming regions of NGC 6822. These observations set the general range of parameters encompassing the physical regime of interest in this thesis. To summarize, typical local disk parameters are a surface density in the range of

[1]The '?' character genuinely is part of the object name.

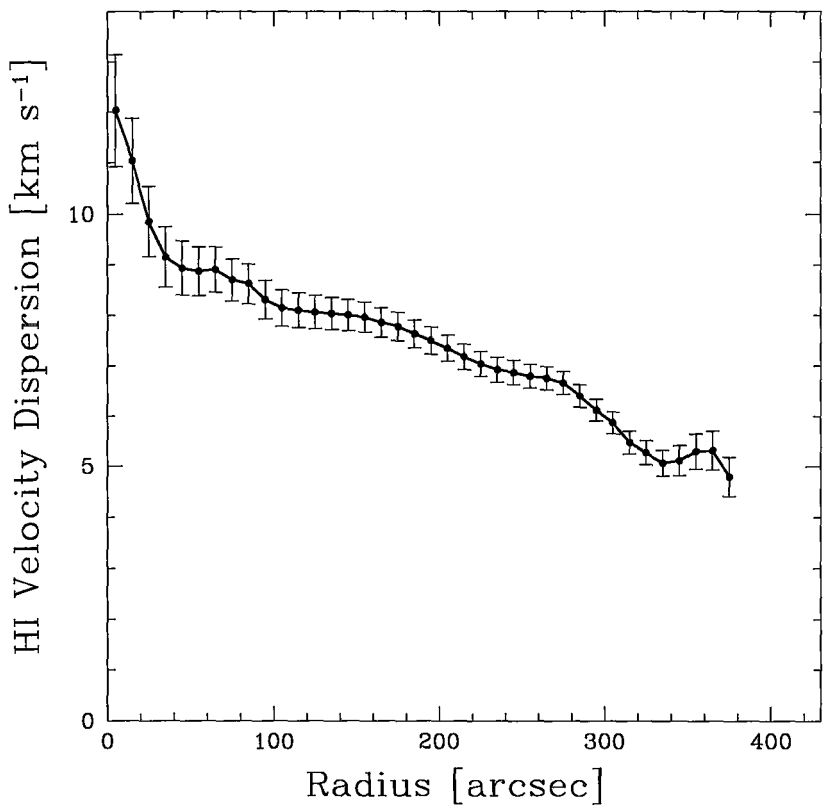

Figure 1.1: HI velocity dispersion in ESO 215-G?009. From Warren et al. (2004) (figure 9). At a distance of 5.25 Mpc, 200″ corresponds to $\approx$ 5 kpc. The Holmberg radius, where the surface brightness in the B band drops below 26.5 mag arcsec^{-2}, is $57.''6 \pm 0.''6$.

$1 - 10\,M_\odot\,pc^{-2}$, a scale height of $500 - 4000$ pc and velocity dispersions on the order of $5 - 10\,km\,s^{-1}$.

1.0.2 The Star Formation Cutoff

The region of star formation is important as it is thought that where star formation happens at a significant rate it is the primary source of energy for driving turbulence (Mac Low and Klessen, 2004). This thesis is focused on the region in a galactic disk beyond where this happens. Generally, the

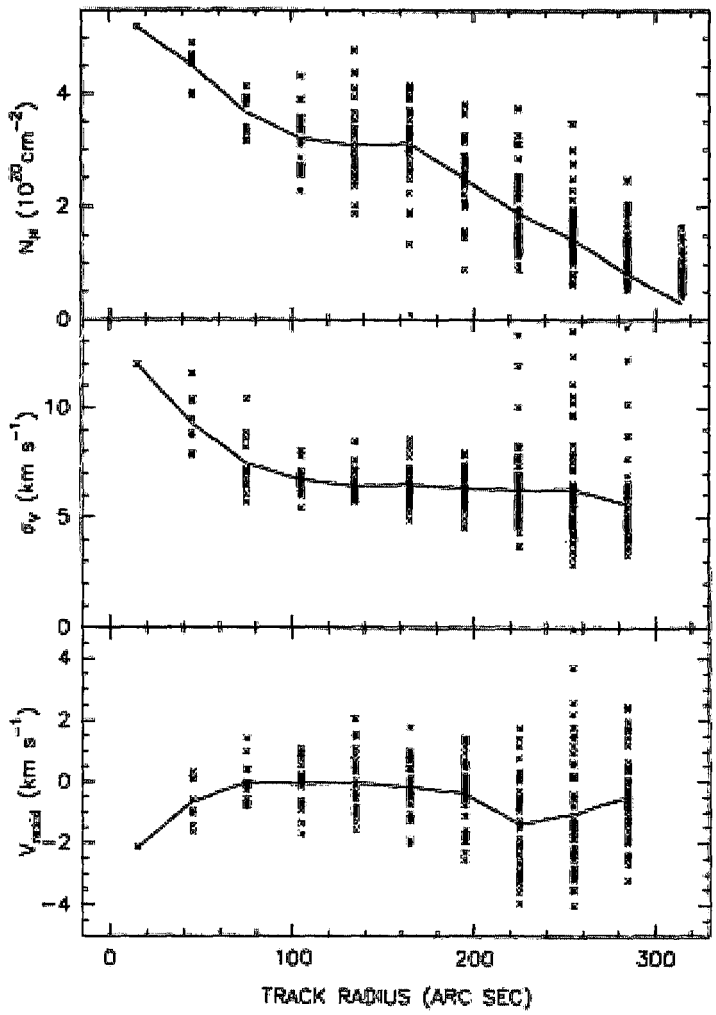

FIG. 3.—Radial dependence of the H I line parameters. Symbols show values for individual sectors, while the lines join the mean values for each radial track. At the top is the column density of H I, traced by the surface brightness of the H I line; in the middle is the Gaussian line width, σ_v; and at the bottom is the residual velocity (i.e., the difference between the line-center velocity and the rotation model). High values of σ_v at large radii correspond to regions of low surface brightness where the line parameters are poorly determined. For radii greater than 270" many sectors contain less than the detection threshold value of 2.7×10^{19} cm^{-2}; they are not plotted individually, but of course they are included in the calculation of the mean N_H.

Figure 1.2: HI in NGC 1058, from Dickey et al. (1990) (figure 9).

star formation rate is highest at the center of a galaxy and decreases with increasing radius. The same trend holds with surface brightness. The most common form of the decrease in surface brightness is a double exponential where surface brightness decreases at some rate until a certain radius, then decreases at a second faster rate(Pohlen et al., 2007). This turn from one rate to another is variously described as a break radius, truncation radius or cutoff. The degree to which this cutoff is sharp varies from galaxy to galaxy. In the simplest interpretation, the star formation rate should vary in the same way as the surface brightness. For producing a sharp cutoff in star formation, the threshold theories of Kennnicutt (1989), Elmegreen and Parravano (1994) and Schaye (2004) offer an explanation through a criterion for the triggering of an instability leading to star formation in terms of large scale parameters. These criteria, respectively the average Toomre Q stability parameter and surface density, pass come critical value, leading to star formation. It is likely the case that, through local compressions and cooling, the conditions for star formation can be met in small areas outside the radius where the large scale parameters are appropriate, this could naturally produce a stronger decline in star formation past the cutoff or break (Elmegreen and Hunter, 2006). Additionally, it has recently been proposed that the total star formation has only a single rate of decline with radius in the galaxy, and that the surface brightness profile with a cutoff is a result of secular evolution of an existing stellar disc (Debattista et al., 2006). This thesis focuses on the region of the galactic disk where the star formation rate has fallen to a level such that the contribution to the gas dynamics from supernovae and other stellar feedback is small. That the transition is not necessarily sharp should, however, be kept in mind.

1.0.3 The Origin of HI Velocity Dispersion

A number of different mechanisms have been proposed for driving the observed HI velocity dispersion past the radius where stars become scarce:

- thermal instability
- infalling clouds
- magnetohydrodynamical instabilities
- self-gravitational instabilities

Sellwood and Balbus (1999) provided a first attempt to explain the observed HI velocity dispersion in the outer regions of NGC 1058 by invoking magnetorotational instability turbulence driven motions of cool clouds. Their analysis does not examine the energy input from self-gravity, instead attempting to argue the disk is sufficiently stable against the self-gravitational amplification of linear perturbations to impede this. Other work dealing with magnetohydrodynamic instabilities and self-gravitational instabilities will be discussed in §1.2.

A number of recent works have addressed the effect of thermal instability (see §1.1.2) in driving turbulent motions in the interstellar medium (ISM; for example Sánchez-Salcedo et al. 2002 and Kritsuk and Norman 2002). The effect of thermal instability on its own has been revisited by Brandenburg et al. (2007) who examine the possibility of thermal instability driving turbulence in ISM-like conditions without stratification or self-gravity, and with and without shear (differential rotation) in a local periodic model. The conclusion of these studies of thermal instability has been that thermal instability does not lead to

sustained turbulence as the cold clouds coalesce. Even with shear these clouds do not break up again in such a way to allow a new phase of coalescence.

The infall of high velocity clouds (HVCs) or intermediate velocity clouds (IVCs) driving gas motions has been examined in Santillan et al. (2007). The conclusion is that HI velocity dispersions of $3 - 8$ km s^{-1} are possible at rates of accretion similar to those observed for the Milky Way (1 $M_\odot$ yr^{-1}). This mechanism is significantly different from others in that it does not arise from processes inside the disk, but from perturbations in a flow accreting onto the disk.

1.1 Basic Physics

This thesis focuses on mechanisms that derive the energy needed to drive gas motions from the gravitational potential energy of the galactic gas. To extract this energy from orbiting gas, it is necessary to move mass inwards, which implies an outward transport of angular momentum. This section does not contain a complete listing of all possible physics which may be important (notably, magnetic fields are omitted) but concentrates on the mechanisms which will be examined in this thesis.

1.1.1 Gasdynamics

The Euler equations, describing the motion of a compressible inviscous gas with terms added for body forces and radiative cooling, are:

$$\frac{\partial \rho}{\partial t} + \nabla \cdot \rho \mathbf{v} = 0 \tag{1.1}$$

$$\frac{\partial \mathbf{v}}{\partial t} + (\mathbf{v} \cdot \nabla)\,\mathbf{v} + \frac{\nabla P}{\rho} = -\nabla \Phi_{ext} - \nabla \Phi_{sg} \tag{1.2}$$

$$\frac{\partial \rho E}{\partial t} + \nabla \cdot [(\rho E + P)\mathbf{v}] = -\rho \mathcal{L}(T) + \rho \mathbf{v} \cdot (-\nabla \Phi_{ext} - \nabla \Phi_{sg}) \tag{1.3}$$

where ρ is the gas density, t is time, $\mathbf{v}$ is velocity, P is pressure, $\mathcal{L}(T)$ is the net heat loss function, Φ_{ext} is an externally imposed gravitational potential, and Φ_{sg} is the self gravitational potential. The self gravitational potential is related to the gas density by Poisson's equation,

$$\nabla^2 \Phi_{sg} = 4\pi G \rho. \tag{1.4}$$

where G is Newton's constant. The total energy E is defined by

$$E = \epsilon + \frac{1}{2}|\mathbf{v}|^2, \tag{1.5}$$

where the internal energy ϵ is related to pressure by the ideal gas equation of state

$$P = (\gamma - 1)\rho\epsilon. \tag{1.6}$$

In this work $\gamma = \frac{5}{3}$, appropriate for galactic gas. Temperatures are obtained from the ideal gas law

$$P = \frac{\mathcal{R}}{\mu}\rho T, \tag{1.7}$$

with mean molecular mass $\mu = 0.62$, appropriate for fully ionized gas of solar metallicity and ideal gas constant $\mathcal{R} = 8.3145 \times 10^7$ cm^2 s^{-2} K^{-1}. The equation of state implies a sound speed c_s of

$$c_s^2 = \frac{\gamma \mathcal{R} T}{\mu}, \tag{1.8}$$

which completes the description of the gasdynamics used.

1.1.2 Thermal Instability

Diffuse gas is, to a good approximation, optically thin. This allows the definition of a net heat-loss function $\mathcal{L}(T)$ which has been added as a sink term the the energy equation (1.3). Field (1965) discusses criteria by which this term will cause an instability leading the gas to locally condense. The instability exists for isobaric perturbations when

$$\left(\frac{\partial \mathcal{L}}{\partial T}\right)_P = \left(\frac{\partial \mathcal{L}}{\partial T}\right)_\rho - \frac{\rho_0}{T_0}\left(\frac{\partial \mathcal{L}}{\partial \rho}\right)_T < 0 \tag{1.9}$$

and exists for isochoric perturbations when

$$\left(\frac{\partial \mathcal{L}}{\partial T}\right)_\rho < 0. \tag{1.10}$$

Mac Low and Klessen (2004) point out that when writing the net heat-loss function

$$\mathcal{L}(T) = \rho \Lambda(T) - \Gamma \tag{1.11}$$

with Γ constant, and $\Lambda(T)$ as a piecewise function in the form

$$\Lambda(T) = C_{i,i+1} T^{\beta_{i,i+1}}, \; T \in [T_i, T_{i+1}], \tag{1.12}$$

for the series of temperature ranges $[T_i, T_{i+1}]$, isobaric instability occurs when $\beta_{i,i+1} < 1$ and isochoric instability occurs when $\beta_{i,i+1} < 0$.

The most unstable scale for thermal instability is referred to as the Field length λ_F (Field 1965; Begelman and McKee, 1990):

$$\lambda_F \equiv \sqrt{\frac{\kappa(T) T}{\rho \max\left(\rho \Lambda(T), \Gamma\right)}} \tag{1.13}$$

where $\kappa(T)$ is the conductivity of the gas. Conduction sets the minimum scale where thermal instability acts. This will play a large role in determining how any simulation involving thermal instability will form structure. The instability will amplify fastest at the smallest resolved scale. In the context studied in this thesis, at the highest stable pressure and density of the warm phase as defined by the cooling function of §2.2 and with an appropriate value for the conduction of $\kappa = 2.5 \times 10^3 T^{1/2}\,\mathrm{cm^{-1}\,K^{-1}\,s^{-1}}$ (Parker, 1953), the Field length is $\lambda_F = 1.2 \times 10^3\,\mathrm{pc}$.

When the form of $\mathcal{L}(T)$ allows two stable temperatures at a single pressure, thermal instability can result in a two-phase medium, where the gas separates into a part at the low stable temperature and the high stable temperature. The form of $\mathcal{L}(T)$ for galactic gas typically has this form in the temperature range of $10 - 10^5\,\mathrm{K}$. In the context of a galactic gas disk, if starting from low density and increasing the surface density, there will be some density at which the pressure at the mid-plane of the disk is high enough for thermal

instability to occur. This minimum pressure has been examined as a criterion to predict the edge of the stellar component of a galactic disk by Elmegreen and Parravano (1994) and Schaye (2004), where the latter concludes that the surface density necessary for the formation of the cool phase should set the position of the star formation cutoff.

1.1.3 Jeans Instability

The Jeans instability criterion (see e.g. Binney and Tremaine, 1987) gives the minimum scale at which self-gravitating gas is unstable to collapse – that is the scale where gravity will overcome the pressure enhancement of a small compression. The three dimensional version of the Jeans length λ_J for gas can be written as

$$\lambda_J \equiv c_s \sqrt{\frac{\pi}{G\rho}}, \tag{1.14}$$

For a thin sheet, the two dimensional Jeans length is

$$l_J \equiv \frac{2c_s^2}{\pi G \Sigma} \tag{1.15}$$

where Σ is the surface density. The Jeans instability will dominate when densities grow large and correspondingly temperatures and sound speeds are low. These conditions often coincide with those for the Toomre Instability as characterized below. At the highest stable pressure and density of the warm phase as defined by the cooling function used in this thesis (see §2.2) the Jeans length is $\lambda_J = 2.7\,\mathrm{kpc}$. At the highest temperature and density in the cold stable phase as defined by the same cooling function, the Jeans length is $\lambda_J = 117\,\mathrm{pc}$.

1.1.4 Toomre Instability

Toomre (1964) examined the conditions for a differentially rotating disk to be unstable to linear axisymmetric perturbations. When the Toomre Q parameter is less than the critical value, the disk is locally unstable to axisymmetric perturbations, and when the Toomre Q parameter is greater than the critical value, the disk is locally stable to axisymmetric perturbations. Gaseous and stellar disks are locally stable to all local linear non-axisymmetric perturbations (Binney and Tremaine, 1987). For a gas disk, the Toomre Q parameter is

$$Q \equiv \frac{\kappa c_s}{\pi G \Sigma} \tag{1.16}$$

where κ is the local epicyclic frequency, $\kappa = (Rd\Omega^2/dR + 4\Omega^2)$ (Binney and Tremaine, 1987). For a finite thickness isothermal disk, the region of stability to axisymmetric perturbations is $Q > 0.676$ (Goldreich and Lynden-Bell, 1965a). The critical (most unstable) wavelength for axisymmetric perturbations in a gas disk is:

$$\lambda_{\rm crit} = \frac{c_s^2}{G\Sigma}. \tag{1.17}$$

Although gas disks are locally stable to non-axisymmetric perturbations, they do respond to such perturbations. In the original treatment of this topic Goldriech and Lynden-Bell (1965b) point out that this may provide a path to convert energy from differential rotation by forming spiral waves to local motions and ultimately to shocks in the interstellar gas.

1.1.5 Angular Momentum Transport

A quiescent shearing gas flow on the scale of the galaxy will not transport any significant angular momentum as there is effectively no viscosity. The transport of angular momentum thus relies on perturbations of some sort in the flow.

The fundamentals of how density perturbations in a disk can transport angular momentum through gravitational coupling, and hence bring the system to a state with lower potential energy are laid out in Lynden-Bell and Kalnajas (1972). Consider an arbitrary galactic disk in cylindrical coordinates (R, ϕ, z) centered at the center of mass. Dividing the galactic disk with a right cylinder at some galactocentric radius, R (position vector $\mathbf{R}$), write down a torque couple $\mathbf{C}$ across this surface:

$$\mathbf{C} = \int \mathbf{R} \times \mathbf{T} \cdot d\mathbf{S} \tag{1.18}$$

in terms of the rank 2 stress tensor $\mathbf{T}$ across this surface. That part relevant to the outward transport of angular momentum is only the z-component of $\mathbf{C}$. Hence, due to the form of equation (1.18) it is only necessary to only analyze the $R\phi$ component of the stress tensor $\mathbf{T}$. The stress tensor $\mathbf{T}$ defined in Lynden-Bell and Kalnajas (1972) and Sellwood (1999) has terms arising from all mechanisms of angular momentum transport. Here a form with a hydrodynamic term and a self-gravity term will be considered. The hydrodynamic term, or Reynolds stress, is of the form $\rho u_R u_\phi$ where ρ is the fluid density and u_R, u_ϕ are the radial and azimuthal component of the fluid velocity vector. The self-gravity term, or Newton stress, is of the form $\rho u_{GR} u_{G\phi}$. This captures the coupling through gravitational attraction of density perturbations

inside and outside the dividing surface. The definition

$$\mathbf{u}_G \equiv \frac{\nabla\Phi}{\sqrt{4\pi G\rho}} \tag{1.19}$$

is introduced as the gravitational velocity following Sellwood and Balbus (1999). The final form of the $R\phi$ component of the stress tensor is

$$T_{R\phi} \equiv \langle \rho u_R u_\phi + \rho u_{GR} u_{G\phi} \rangle. \tag{1.20}$$

Substituting back into the definition of the torque couple, and taking the z-component contribution gives:

$$C_z = \int \left(\rho u_R u_\phi + \frac{1}{4\pi G} \left(\nabla\Phi\right)_\phi \left(\nabla\Phi\right)_R \right) \, dS, \tag{1.21}$$

the gravity component of this is simply

$$C_{Gz} = \frac{1}{4\pi G} \int \left(\nabla\Phi\right)_\phi \left(\nabla\Phi\right)_R \, dS. \tag{1.22}$$

So, if it is required that the gravitational torque couple move the disk towards lower potential energy, then C_{Gz} must be positive, hence the perturbation self-gravity forces $\left(\nabla\Phi\right)_\phi$ and $\left(\nabla\Phi\right)_R$ must have on average a leading spiral configuration so that the integral C_{Gz} is positive. The Poisson equation demands that the direction of the self-gravity forces are perpendicular to the isopotential contours and the isodensity contours. Due to the leading spiral requirement on the perturbation gravity forces, the self-gravitational isopotential and isodensity contours must then have a trailing spiral form on average (Lynden-Bell and Kalnajs, 1972).

The effect of this torque couple is to transfer energy from the rotation of the disk to local motions of the gas (Sellwood and Balbus, 1999). The rate at which this energy is transferred can be expressed as:

$$\dot{e}_{supply} = -\frac{d\Omega}{d\ln R}\langle T_{R\phi}\rangle, \tag{1.23}$$

which for a flat rotation curve is:

$$\dot{e}_{supply} = \Omega\langle T_{R\phi}\rangle. \tag{1.24}$$

A second useful formulation of this basic rate is given by Balbus and Papaloizou (1999), where for some quantity X the average is defined as

$$\langle X\rangle_\rho \equiv \frac{1}{2\pi\Sigma\Delta R}\int_{-\infty}^{\infty}\int_{R-\Delta R/2}^{R+\Delta R/2}\int_0^{2\pi} \rho X \; d\phi \; dR \; dz \tag{1.25}$$

and the radial component of $\mathbf{T}/\rho$ is denoted as $W_{R\phi}$. Then the rate of energy dissipation per unit area (which would be the luminosity in an accretion disk) is

$$Q_e = -\Sigma\langle W_{R\phi}\rangle_\rho \frac{d\Omega}{d\ln R} \tag{1.26}$$

This energy release is associated with the movement of mass deeper into the potential well of the galaxy. The result of the redistribution of mass in the disk to smaller radii leaves the mass which has moved inward with less angular momentum and lower potential energy.

The rate at which mass moves inwards can be estimated as follows. First, consider the magnitude of angular momentum L of a mass m at radius

r rotating on a flat rotation curve Ω

$$L = mr^2\Omega(r) = mr^2\frac{\Omega_{r_0}r_0}{r} \tag{1.27}$$

differentiating at radius r_0, assuming a constant orbital velocity (flat rotation curve) and that mass is conserved,

$$\frac{dL}{dt} = m\Omega_{r_0}\frac{dr}{dt}. \tag{1.28}$$

The left hand side of this expression is related to the stress tensor, the volume average of dL/dt is the volume average of the $R\Phi$ component of the stress tensor $\langle T_{r\phi}\rangle_V$. To make the replacement in the left hand side, a similar change to the right hand side, replacing m with the density-weighted average volume density defined

$$\langle\rho\rangle_\rho \equiv \frac{\int \rho^2 dV}{\int \rho dV} \tag{1.29}$$

is made. This expression can then be slightly rearranged to give

$$\langle\rho\rangle_\rho\frac{dr}{dt} = \langle T_{r\phi}\rangle_V\frac{1}{\Omega}. \tag{1.30}$$

To get to a mass accretion rate in dimensions of $[M/T]$ it is necessary to multiply by the lengths over which the azimuthal and vertical directions of the integrations which have been preformed in the averaging. The azimuthal dimension is the circumference at radius r_0 or $2\pi r_0$. To get the vertical dimension, the fact that a surface density Σ can usually be obtained can be used to define a vertical scale H,

$$H \equiv \frac{\Sigma}{\langle\rho\rangle_\rho}. \tag{1.31}$$

Multiplying through by $2\pi r_0 H$ a mass accretion rate is obtained as

$$\dot{M} = \langle T_{r\phi} \rangle_V \frac{2\pi r_0 H}{\Omega_{r_0}}. \tag{1.32}$$

Importantly, in simulations all the parameters on the right hand side of this expression can be directly evaluated.

1.1.6 A Basic Estimate

With the material presented so far, the foundation exists to examine a simple estimate of the ability of self-gravity to power turbulent motions. In a review aimed at star formation, Mac Low and Klessen (2004) attempt to examine the possible role in galactic disks of self-gravity driven turbulence. Mac Low and Klessen (2004) give, in their equation (42), an approximate rate for the energy dissipation rate of isothermal turbulence

$$\dot{e}_{\text{dissipation}} \simeq -\frac{1}{2}\rho v_{rms}^3 L_d^{-1} \tag{1.33}$$

$$\simeq -\left(3 \times 10^{-27} \text{ erg cm}^{-3} \text{ s}^{-1}\right) \times \left(\frac{n}{1 \text{ cm}^{-3}}\right)\left(\frac{v_{rms}}{10 \text{ km s}^{-1}}\right)^3 \left(\frac{L_d}{100 \text{ pc}}\right)^{-1}, \tag{1.34}$$

where ρ is the average density, v_{rms} is the RMS velocity dispersion, and L_d is the driving scale of the turbulent cascade. To evaluate the viability of self-gravity to drive an analogous estimate is needed for the energy supply rate from self gravity. This can be derived by returning to the Lynden-Bell and Kalnajas (1972) formulation of the Newton stress $T_{R\Phi} = \langle \rho u_{GR} u_{G\Phi} \rangle$. Approximately evaluating this expression, Mac Low and Kelssen (2004) and Wada et al. (2002) find as an estimate as the size of the energy input from the

Newton stress:

$$\dot{e}_{\rm supply} \simeq G\left(\frac{\Sigma_g}{H}\right)^2 \lambda^2 \Omega \tag{1.35}$$

$$\simeq \left(4\times10^{-29}\ {\rm erg\ cm^{-3}\ s^{-1}}\right) \times\left(\frac{\Sigma_g}{10\ {\rm M_\odot\ pc^{-2}}}\right)^{-2}\left(\frac{H}{100\ {\rm pc}}\right)^{-2} \times\left(\frac{\lambda}{100\ {\rm pc}}\right)^2\left(\frac{\Omega}{(220\ {\rm Myr})^{-1}}\right), \tag{1.36}$$

where Σ_g is the surface density of the disk, H is the scale height of the disk, λ is the Jeans length in the disk, and Ω is the angular velocity. The values chosen in equations (1.34) and (1.36) are appropriate for the solar neighborhood in the Milky Way. At least in that context, $\dot{e}_{\rm supply}$ is two orders of magnitude smaller than $\dot{e}_{\rm dissipation}$, as noted by Mac Low and Klessen (2004).

By combining these estimates of supply and dissipation, it is possible to examine how self-gravity can be favored or disfavored in different contexts. The argument that follows is original to this thesis. Equating the approximate density ρ in $\dot{e}_{\rm dissipation}$ to the density term Σ_g/H in $\dot{e}_{\rm dissipation}$ and then equating the length sales L_d and λ in the same expressions. The ratio between the rates of energy supply and dissipation then can be expressed as:

$$\frac{\dot{e}_{\rm supply}}{\dot{e}_{\rm dissipation}} \approx 2G v_{rms}^{-3}\Omega\rho\lambda^3. \tag{1.37}$$

Now, consider how this quantity (1.37) would vary with galactic radius. One would expect v_{rms} to slowly fall to a near-constant, Ω to be nearly constant, ρ to fall, and λ to rise. Hence, as (1.37) depends on the third power of λ, a rise in λ with galactic radius can easily cause it to exceed unity, making self-gravity a viable turbulence driving mechanism. Compared to the value at the solar

radius, λ would need to increase by factor of 5 to make (1.37) exceed unity, given the other quantities are held constant.

This discussion of estimated energy supply and dissipation rates from isothermal turbulence and self gravity has a number of problems. Foremost is that a galactic disk is observed to be multiphase, not isothermal. Also, when considering length scales there may be two regimes; when the Jeans length λ is smaller than the scale height H of the disk the system can be considered to be fully three dimensional; however, if λ significantly exceeds H then the system is arguably two dimensional at large scales and three dimensional at small scales. The arguments presented above do not take this into account.

To accurately evaluate the ability of self-gravity to drive turbulence, it is necessary then to proceed further than this simple kind of estimate. Numerical models make it possible to capture the interplay of the geometrical gas structure, phase structure and forces coupling the gas to the differential rotation.

1.2 Numerical Models

Two basic types of models have been used in simulations to attempt to understand the evolution of a galactic gas disk. The general choice is between a computational domain which encloses the entire disk, a global simulation, and a computational domain which encloses only a small part of the disk and enforces an appropriate set of boundary conditions, a local simulation.

There is an additional significant choice to be made about what sort of numerical technique should be used to solve the Euler equations in the model. Here, all the work discussed uses Cartesian coordinates and mesh

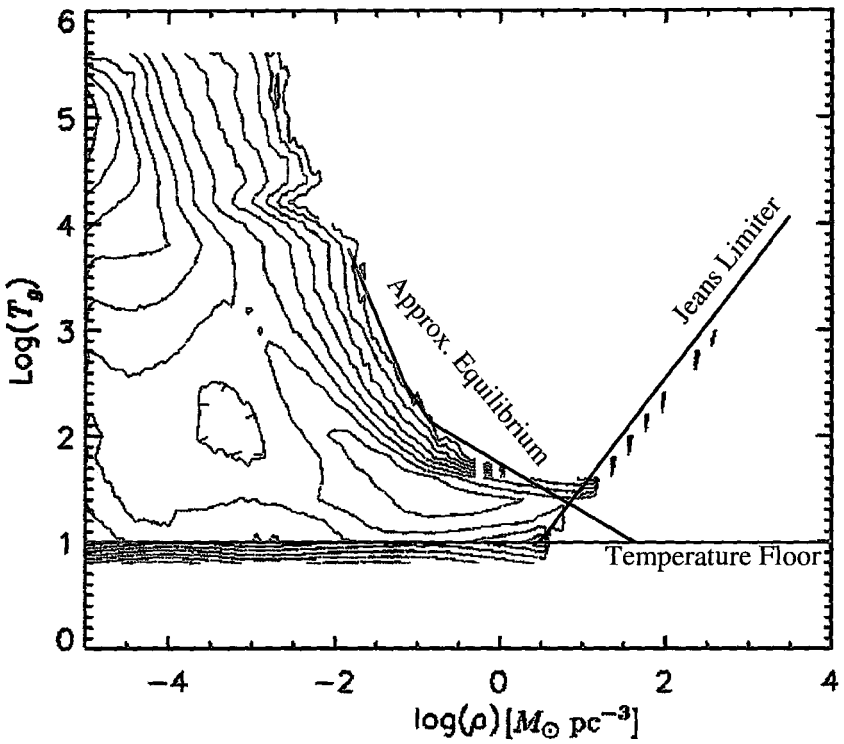

Figure 1.3: Phase diagram from Wada and Norman (2007) (figure 8) with approximate line of heating-cooling equilibrium states, 10 K temperature floor, and Jeans Length limiter over-plotted.

based gasdynamics, none of the work mentioned here uses Lagrangian (e.g. particle) methods.

1.2.1 Global Disk Models

A series of papers (Wada and Norman, 1999; Wada and Norman, 2001; Wada et al., 2002; Wada and Norman, 2007) examine a global disk model of gas in a fixed potential with a specified equilibrium cooling function and constant heating. All but the last of these models are two dimensional and all use a uniform resolution grid with no time step limit from cooling processes. The most relevant result claimed from these is that self-gravity driven turbulence is

found in all the systems examined. Further, the turbulence found is supersonic, and acts to stabilize the disk at $Q \approx 1$. The phase diagram in Wada and Norman (2007) is shown in figure (1.3) with added annotation. Here, the artificial limits on the gas state are plotted, and an approximation to the line of heating-cooling equilibrium solutions is plotted. The function for the equilibrium curve is that from Brandenburg et al. (2007), not that from Wada and Norman (2007) as the latter is not numerically specified. Two aspects of this plot are notable. First that the gas mass is spread over a large temperature range for each density below the equilibrium curve on the heating-unstable side and, second, the presence of dense clouds above the highest resolved density (seen scattered on the Jeans Limiter line). It is claimed that the disks evolve to a quasi-steady gravitoturbuent state.

Tasker & Bryan (2006) also computed global galaxy models, but on a larger physical scale and lower physical resolution than Wada and Norman (2007) with an adaptive mesh gasdynamics code. In their runs without supernova feedback, the resulting structures are qualitatively similar to those in (Wada and Norman, 2001). However, these models do not claim to find a quasi-static turbulent state, and the nature of any turbulence present is not explored.

1.2.2 Local Disk Models

In 2D (razor thin disk assumption) simulations with a fixed cooling time Gammie (2001) and Johnson and Gammie (2003) find a gravitoturbulent quasi-steady state. Their isothermal disks fragment for $Q \lesssim 1.4$ in 2D. For comparison, the critical Q below which the disk is unstable to axisymmetric

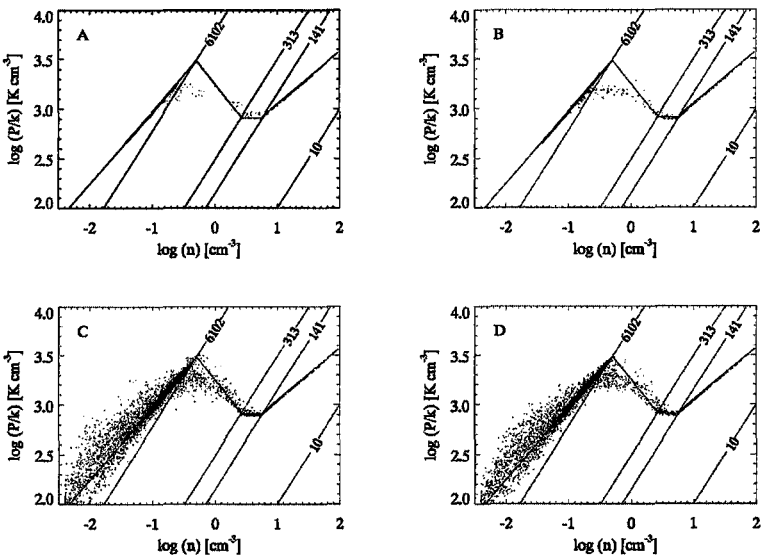

Figure 1.4: Phase diagram from Pinotek and Ostriker (2007) figure (13).

perturbations for a razor thin disk is 1, and for a finite thickness isothermal disk, 0.676 (Binney and Tremaine, 1987). These models are local, but use the local expansion of a Keplerian disk (appropriate for protostellar accretion disk), which has different parameter values then the local expansion appropriate for an outer galactic disk. The 2D model also assumes no vertical-direction structure other than a hydrostatic atmosphere in the disk, which may not be true in the case of a galactic disk. In fixed cooling time simulations, certain values of the cooling time result in a disk in a quasi-steady state of gravitoturbulence. The uniqueness of this state is not explored by Johnson and Gammie.

Pinotek and Ostriker (2007) examine the role of magnetorotational instability (MRI) driven turbulence in a stratified disk with cooling gas. Their local (shearing box) simulations develop a quasi-steady state with supersonic turbulence. These simulations display higher turbulent velocity amplitudes in

the warm gas than in the cool gas. Also, the turbulent velocities are lowest at the mid-plane of the simulated disk. They suggest that these MRI driven velocities can suppress self-gravitational instability inside these clouds, impeding star formation even where cool clouds form.

The use of a local model (specifically a shearing box, see §2.1) implies that is the energy flux will be purely local (Balbus and Papaloizou, 1999). This is not natural in self-gravitating systems, especially disks where low order modes (global spirals, bars) are dominant. Consequently, shearing boxes can not be used in general to study the dynamics of self-gravitating disks. In the context of this thesis, this restriction is in fact a benefit – the shearing box restricts the gravitational feedback to be of a local form. If the shearing box is considered in the context of a galaxy, this allows the examination of mechanisms that may act locally in one part of the the disk independent of the dynamics in other parts. Hence, the mechanisms active in shearing box models must energetically be of a somewhat minimal nature, relying only on local transfers of energy. Further, this implies that mechanisms active in shearing box simulations should have some independence from the global nature of the galaxy. This independence means that shearing box simulations should indicate whether a specific proposed mechanism will function universally across a range of specific galaxies. Conversely, if such simulations show null results, then one of the specific hypothesis that can be tested in the future is that the proposed mechanism must function on global scales to be active.

Chapter 2

Methods

A local model for a stratified differentially rotating disk has been implemented through modifications of FLASH 2.3r1[1] (Fryxell et al., 2000). FLASH is a block-based adaptive mesh refinement (AMR) gasdynamics code with a variety of existing modules for added physics relevant to astrophysical problems. The included physics in the version developed here are gasdynamics, local self-gravity, shear (differential rotation) and either an isothermal equation of state or a ideal gas with a simplified net heat loss term. The result is a set of simulations in the style of Pinotek and Ostriker (2007) which capture the physics of a local version of Wada and Norman (2007). Primarily, this will allow the examination of self-gravitational effects on the system.

A local model, specifically a shearing box, was used with an adaptive mesh for three main reasons. The local model allows higher physical resolution to be achieved with a given computational resource and it allows effects above the box scale to be cut off so that only local mechanisms may be active. With the use of an adaptive mesh, the computational box can be made tall and thin, with a coarse mesh high above the mid-plane and a fine mesh in the mid-plane, where the disk is most dense. This allows for more physical vertical direction

[1] `http://www.flash.uchicago.edu/`

boundaries. The periodic boundaries of the shearing box do however impose a false exact symmetry on the system, excluding the possibility of any net mass transfer and forcing angular momentum transport to be of a purely local manner, as described in §1.2.2.

2.1 Shearing Box

To build a local mode of part of a galactic disk, Hill (1878) shows how to expand the equations of motion for a particle about a circular orbit. Here, the x direction is the radial direction R, y is the azimuthal direction Φ, and z is the vertical direction.

$$\frac{\partial v_x}{\partial t} = 2\Omega v_y + 2q\Omega^2 x \tag{2.1}$$

$$\frac{\partial v_y}{\partial t} = -2\Omega v_x \tag{2.2}$$

$$\frac{\partial v_z}{\partial t} = -\Omega^2 z \tag{2.3}$$

This formulation is adopted from Wisdom and Tremaine (1988). Ω is the angular velocity of the orbit at the center of the shearing box and q is defined as $q = -d\ln\Omega/d\ln R$. For a Keplerian disk $q = \frac{3}{2}$ and for a flat rotation curve such as occurs in the outer regions of a galactic disk $q = 1$. To build a local model, periodic boundary conditions are needed in the radial and azimuthal directions, however the radial direction case is complicated by the differential rotation. To solve this difficulty a shearing-periodic boundary is introduced in the x direction. For a variable f and a shearing-box size L this shear-periodic

Table 2.1: Parameters of the Shearing Bar Test

Parameter	Value
Box Size	0.5 cm
Number of cells	32×32
γ	$\frac{5}{3}$
Ambient Density	5.0×10^{-7} g cm^{-3}
Initial Bar Width	2 cells
Initial Bar Density	5.5×10^{-7}
Initial Pressure	1.8×10^{5}
Ω	10^{3}
q	1.5
Output Time	454 s

mapping is (Hawley et al., 1995)

$$f(x, y, z) = f(x + L, y - q\Omega L t, z). \tag{2.4}$$

As this implies that the points where variables are mapped moves in time; y velocities mapped across the shearing boundary are altered as (Hawley et al., 1995)

$$v_y(x, y, z) = v_y(x + L, y - q\Omega L t, z) + q\Omega L. \tag{2.5}$$

The y direction boundaries are purely periodic and the z direction boundaries will be discussed in conjunction with the treatment of gravity in §2.4. Due to the differential rotation, a steady state flow in the shearing box must have $v_y = q\Omega x$. This will be referred to as the background flow.

2.1.1 Implementation of the Shearing Box

The ability to split the steady-state background flow in the shearing box is split from the Euler equations has been added to FLASH by modifying

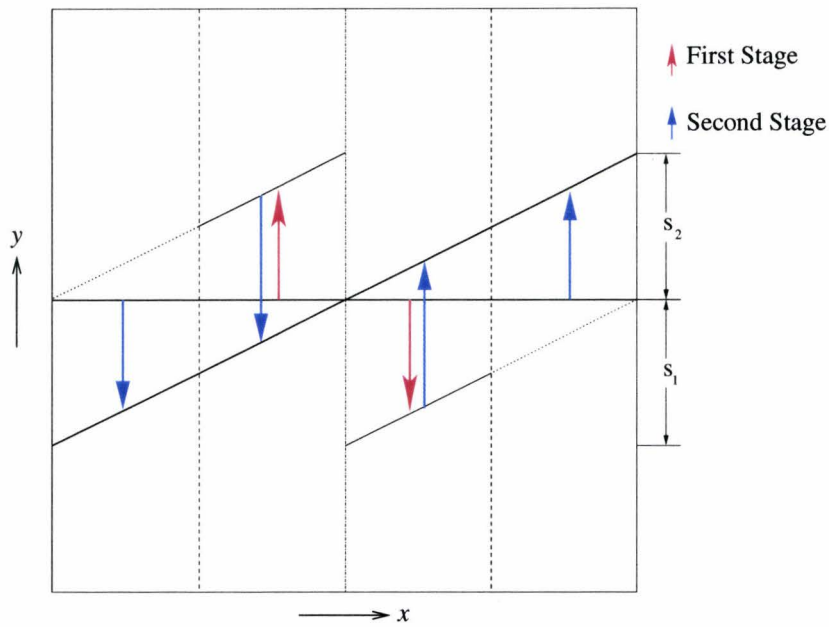

Figure 2.1: Schematic of shifts made by 2-stage y-advection operator

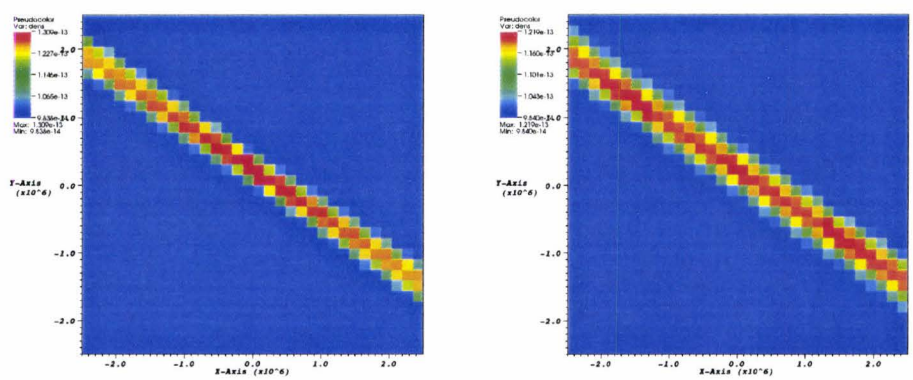

Figure 2.2: *Left:* Thermally unstable density bar without 2-stage y-advection, center-edge difference in peak density is 4.1%. *Right:* Same as left panel but with 2-stage y-advection, the center-edge difference in peak density is 1.9%.

the y-sweep of the directionally split PPM hydrodynamics scheme. Instead of solving the y-direction gasdynamic equations with the full velocity the fluid is advected using a PPM interpolation and the Euler equations are solved in the frame comoving with the background flow. This is very similar to the methods of Masset (2000) and Gammie (2001). The limiting time step constraint is usually not the gasdynamic Courant-Friedrichs-Lewy condition, but the limit of the cooling time limit. Hence, even for cells near the x extrema of the box, many time steps are taken in the time that it takes for a fluid element to cross a cell. However, due to the background shearing flow, the fluid gas is on average moving faster across the grid at the edges then the center. This means that many more time steps are taken for a fluid element to cross a cell in the center of the box than for a fluid element to cross a cell at the edge of the box. The result is that the numerical diffusion near the edges of the grid is much greater than in the center. This is dangerous, as the thermal instability evolution of a clump depends strongly on the density of a clump, and under these conditions clumps are more smeared out at the edges of the gird (see for example the left panel of figure 2.2). If this difference is strong enough, the simulation will develop a strong artificial perturbation at the box scale, invalidating the local nature of the simulation. To combat this, a new scheme for y-advection has been developed. Two regimes of advection are introduced; in the center region of the box, gas is advected a small distance by advecting forwards a large distance and then reverse large distance and near the edges gas is only advected forwards. The effect of this is to introduce a similar numerical diffusion into the advection in the center of the box as exists near the edges. A diagram of this procedure is shown in figure (2.1). In this discussion, a terminology of shifts is used to mean the maximum distance

material is advected by at the edge of the region in question. The actual distance shifted varies linearly across the box, as indicated for each shift in the diagram. Specifically, the advection is done in two stages, in the first stage, the center half of the box is shifted forwards with a shift s_1, in the second stage, the outer half of the box is shifted forwards by a shift s_2 and the center half of the box is shifted back $s_2 - s_1$. Thus the net shift everywhere is s_2. The ratio of s_2 to s_1 is a tuned parameter set to 2.

In addition to the y-advection, it is necessary at each time step to change the logical geometry of this grid to follow the shearing motion of the x boundary. That is, the shift used to map the cells at the periodic boundary is changed, and the internal data structures added to FLASH to facilitate the shearing boundary must be updated. This operation is referred to as slide edge in the following discussion. The PPM hydrodynamics implemented in FLASH uses a series of one-dimensional solutions to build the three-dimensional gas-dynamics, in a technique known as Strang splitting (Strang, 1968). In effect, along with the y direction PPM solve and y advection operator the slide edge operation is part of the larger y direction gasdynamic operator that forms one of the units to which the Strang splitting is applied.

In the version Strang splitting used by the FLASH PPM implementation, there are two sets of one-dimensional gasdynamics calls: first one-dimensional PPM solutions are preformed in the order x,y,z; and then z,y,x. To include the y-advection operator and shearing boundary, this is modified to x, y-advection, y, y-advection, slide edge, z and z, y-advection, y, y-advection, slide edge, x. Figure (2.2) shows the evening effect of this 2-stage y-advection on the evolution of a shearing thermal instability. The initial condition is an isobaric bar, as specified in Table (2.1).

Due to data locality constraints following from the FLASH framework, a 3-point stencil is used to interpolate values on the shearing boundary. This procedure uses the same reconstruction polynomial as PPM, but assigns the cell-edge values in a way that only uses 3 adjacent cell values (not 5 as in PPM) and does not make the reconstruction piecewise continuous in smooth regions as in PPM.

The basic quadratic polynomial used for the reconstruction is the same as in PPM:

$$a(x) = a_L + x\left(\Delta a + a_6(1-x)\right), \quad x \in [0,1]. \tag{2.6}$$

The parameters a_L, Δa, a_6 are determined in a similar manner to that used in PPM, but with a smaller stencil. The left and right interface slopes $\delta_{+\frac{1}{2}}$ and $\delta_{-\frac{1}{2}}$ are determined by the centered differences

$$\delta_{+\frac{1}{2}} = \langle f\rangle_1 - \langle f\rangle_0 \tag{2.7}$$

$$\delta_{-\frac{1}{2}} = \langle f\rangle_0 - \langle f\rangle_{-1}. \tag{2.8}$$

To guarantee monotonicity of the interpolation, the interpolant must be flattened if this cell contains a local maxima.

$$\text{if } (\delta_{+\frac{1}{2}}\delta_{-\frac{1}{2}}) \leq 0 \text{ then } \delta_{+\frac{1}{2}} \to 0,\ \delta_{-\frac{1}{2}} \to 0 \tag{2.9}$$

Further, as in PPM overshoots must be cut off by limiting the larger of the two slopes

$$\text{if } \left((\langle f\rangle_{-1} \leq \langle f\rangle_0) \text{ and } (\langle f\rangle_0 \leq \langle f\rangle_1) \text{ and } \left(\left(\frac{\delta_{-\frac{1}{2}}}{\delta_{+\frac{1}{2}}}\right) > \frac{1}{4}\right)\right) \text{ then } \delta_{+\frac{1}{2}} \to 4\delta_{-\frac{1}{2}}, \tag{2.10}$$

$$\text{if } \left((\langle f \rangle_{-1} \leq \langle f \rangle_0) \text{ and } (\langle f \rangle_0 \leq \langle f \rangle_1) \text{ and } \left(\left(\frac{\delta_{+\frac{1}{2}}}{\delta_{-\frac{1}{2}}} \right) < \frac{1}{4} \right) \right) \text{ then}$$
$$\delta_{-\frac{1}{2}} \rightarrow \frac{1}{4}\delta_{+\frac{1}{2}}, \quad (2.11)$$

$$\text{if } \left((\langle f \rangle_{-1} \geq \langle f \rangle_0) \text{ and } (\langle f \rangle_0 \geq \langle f \rangle_1) \text{ and } \left(\left(\frac{\delta_{+\frac{1}{2}}}{\delta_{-\frac{1}{2}}} \right) > \frac{1}{4} \right) \right) \text{ then}$$
$$\delta_{-\frac{1}{2}} \rightarrow 4\delta_{+\frac{1}{2}}, \quad (2.12)$$

$$\text{if } \left((\langle f \rangle_{-1} \geq \langle f \rangle_0) \text{ and } (\langle f \rangle_0 \geq \langle f \rangle_1) \text{ and } \left(\left(\frac{\delta_{-\frac{1}{2}}}{\delta_{+\frac{1}{2}}} \right) < \frac{1}{4} \right) \right) \text{ then}$$
$$\delta_{+\frac{1}{2}} \rightarrow \frac{1}{4}\delta_{-\frac{1}{2}}. \quad (2.13)$$

With these limited slopes, the right and left interface values of the interpolating parabola are defined as

$$a_R \equiv \frac{1}{3}\delta_{+\frac{1}{2}} + \frac{1}{6}\delta_{-\frac{1}{2}} \quad (2.14)$$
$$a_L \equiv -\frac{1}{6}\delta_{+\frac{1}{2}} - \frac{1}{3}\delta_{-\frac{1}{2}} \quad (2.15)$$

these are limited to ensure monotonicity, as in PPM (Colella and Woodward 1984, equation (1.10))

$$\text{if } (a_R - a_L)\left(\langle f \rangle_0 - \frac{1}{2}(a_L + a_R) \right) > \frac{(a_R - a_L)^2}{6} \text{ then}$$
$$a_L \rightarrow 3\langle f \rangle_0 - 2a_R \quad (2.16)$$
$$\text{if } (a_R - a_L)\left(\langle f \rangle_0 - \frac{1}{2}(a_L + a_R) \right) < -\frac{(a_R - a_L)^2}{6} \text{ then}$$
$$a_R \rightarrow 3\langle f \rangle_0 - 2a_L. \quad (2.17)$$

Table 2.2: Coefficients for the Cooling Curve

i	T_i	$C_{i,i+1}$	$\beta_{i,i+1}$
1	10	3.70×10^{16}	2.12
2	141	9.46×10^{18}	1.00
3	313	1.185×10^{20}	0.56
4	6102	2×10^{8}	3.67
5	10^5	7.96×10^{29}	−0.65

Finally, the same definitions of parameters from PPM (Colella and Woodward, 1984) are used,

$$\Delta a \equiv a_R - a_L \tag{2.18}$$

$$a_6 \equiv 6\left(\langle f\rangle_0 - \frac{1}{2}(a_L + a_R)\right). \tag{2.19}$$

Cells are mapped across the shearing periodic boundary by constructing the polynomial equation (2.6) and averaging it over the required interval. As with the interpolation at grid interfaces in adaptive meshes, this interpolation does not conserve the consistency of the physical quantities with the equation of state, and so the non-conserved physical quantities are corrected based on the conserved subset.

The validity of this implementation of the shearing box boundary conditions and the two-stage y-advection is demonstrated by the tests in §2.5.

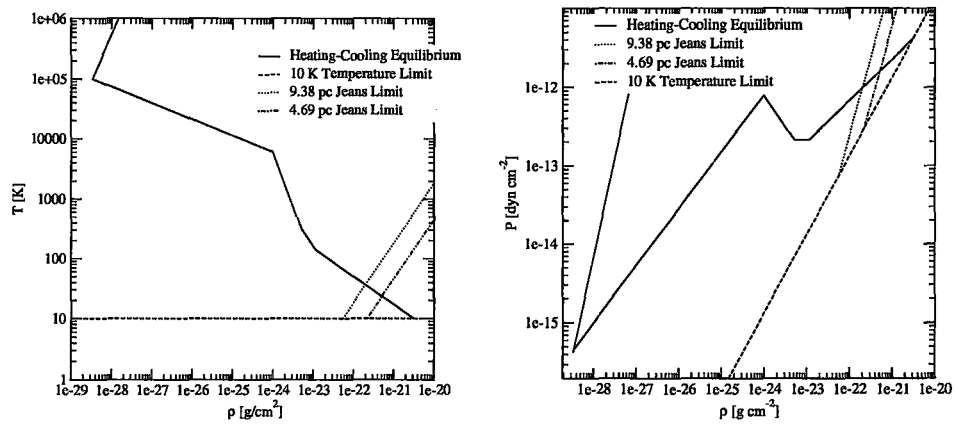

Figure 2.3: Phase diagram showing line of equilibrium heating-cooling solutions, Jeans Length limits (see §2.4.4) and 10 K temperature floor.

2.2 Cooling

To include the local effects of various optically-thin limit cooling and heating mechanisms a net heat loss function is defined:

$$\mathcal{L}(T) = \rho\Lambda(T) - \Gamma \tag{2.20}$$

where Γ is a constant following Brandenburg et al. (2007) and others. The values for the parameters of this function are picked to mimic the action of various physical mechanisms. As this is possibly a very large parameter space to choose from, the primary concern is consistency with related previous work. We use a heating parameter $\Gamma = 0.015\,\mathrm{erg\,g^{-1}\,s^{-1}}$ as in Brandenburg et al. (2007) and Pinotek and Ostriker (2007). The form of $\Lambda(T)$ is a piecewise power law fit from Brandenburg et al. (2007), which is a continuous version of the fit given by Sánchez-Salcedo et al. (2002) which was used by Pinotek and Ostriker (2007)

$$\Lambda(T) = C_{i,i+1}T^{\beta_{i,i+1}},\ T \in [T_i, T_{i+1}]. \tag{2.21}$$

The coefficient values ($C_{i,i+1}$) are given in Table (2.2). A temperature floor of 10 K is used, and resolution of the Jeans length is ensured by an additional temperature limiter of the form used by Wada and Norman (2007) to prevent artificial fragmentation (see §2.4.4):

$$T_{min} = 35 \text{ K } \left(\frac{\rho}{10 \mathrm{M}_\odot \text{ pc}^{-3}}\right) \left(\frac{\Delta}{5 \text{ pc}}\right)^2 . \tag{2.22}$$

Figure (2.3) shows the equilibrium solutions where $\Gamma - \rho\Lambda = 0$.

Numerically, the cooling is split from the other operators, and the cooling equation is integrated for the global time step with an Euler method with a sub-cycle time step of $.05e/\dot{e}$. The global cycle time step is limited proportionally to $e/\dot{e}$, but the limiting factor is between 25 and 1, and this is not chosen to ensure accuracy but to limit the evolution so that the Riemann solver in the PPM stage will converge.

To ensure strict convergence across resolution of the formally thermally unstable regions, Koyama and Inutsuka (2004) argue that it is necessary to resolve the length scale where this instability grows fastest, the Field length. It is suggested that this be accomplished by explicitly including a conduction which is constant at all resolutions and which is much greater then the numerical conduction at all resolutions. However, Gazol et al. (2005) argue that this is a minimal concern when global properties are investigated, and when the numerical conduction is at least enough to stop the smallest resolved scale from also being the most unstable.

2.3 Approximating Isothermal Gas

FLASH does not include an isothermal gas Riemann solver for use in the PPM gasdynamics. To approximate isothermal gas with the standard variable γ FLASH Riemann solver, a γ value of 1.01 is used in conjunction with a cooling operator set to bring the temperature to the specified isothermal temperature. The time step is not limited on the cooling time. This approach is more robust against spurious temperature increases than simply using an approximately isothermal γ over long evolution times. The γ used with this technique is also larger than that which would be required by simply using a $\gamma \approx 1$. From experience, it is found that using larger γ is less likely to result in the FLASH PPM Riemann solver to failing to converge.

2.4 Gravity

The gravitational potential employed consists of two parts, an external part and a part resulting from self-gravity. The external part, Φ_{ext} is a fixed background resulting from the expansion of the effective potential of a circular orbit in Hill's equations (equation (2.3)). The self-gravity part Φ_{sg} is a result of solving the Poisson equation with periodic boundary conditions within the simulation volume.

2.4.1 Self-Gravity

The boundary conditions used for self-gravity in the x and y directions are the same shearing box boundaries as described in §2.1. The basic multigrid solver in FLASH can be used to solve in these boundary conditions

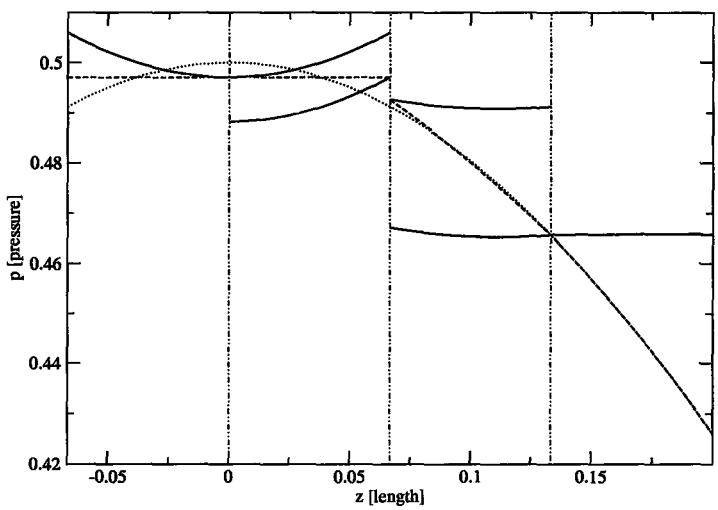

Figure 2.4: Example of errors caused by interaction of PPM hydrostatic gravity modification and monotonicity limiters of PPM interpolation. Cell divisions are indicated by vertical lines, analytic pressure function by dotted line, PPM interpolated pressure reconstruction by dashed lines, corrected left pressure states by thick red lines, and corrected right pressure states by thick blue lines.

without modification, other then patching a bug affecting the filling of guard cells during the pre- and post- V-cycle smoothing phase.[2] The top level solve used for the coarse grid does require modification. Originally, FLASH used an FFT-based (Fast Fourier Transform) spectral method to solve Poisson's equation with periodic boundary conditions on the coarse grid. To modify the spectral solution to a skew-periodic boundary, the procedure of Gammie (2001) is followed. The original source term is interpolated to a frame of skew-periodic coordinates, the FFT-based solve is performed in this frame where the equation and boundary conditions are again separable, and the solution is then linearly interpolated back to the original grid. These two linear interpolations do introduce noise into the solution, and this is effectively damped by applying the standard FLASH multigrid smoothing operator on the solution before proceeding with the rest of the V-cycle.

This interpolation error in the FFT solution to the skew-periodic Poisson equation can be avoided. The error arises from the finite order of the interpolation used in the azimuthal direction of the grid. We can, however, exploit the exact periodic nature of the problem in the azimuthal direction; the FFT is first performed on each azimuthal row; the resulting imaginary values are rotated in the imaginary place by an amount appropriate to the shift of that row; and finally the FFT is done in the radial and other directions. This procedure exploits the fact that the FFT on a periodic grid is actually a perfect interpolation.[3]

[2]See `http://imp.mcmaster.ca/~colinm/gpatch/index.html`

[3]This procedure, suggested in a posting on the author of this thesis's website, has been implemented by the authors of THE PENCIL CODE `http://www.nordita.org/software/pencil-code/doc/manual.pdf`

2.4.2 External Potential

The first order expansion about a circular orbit for the vertical background gravitational acceleration in Hill's equations is

$$g = -\Omega^2 z. \tag{2.23}$$

This choice is not appropriate for the Euler equations if periodic z boundary conditions (Fromang and Papaloizou, 2006), or outflow z boundary conditions are used. To make use of an outflow boundary condition in the z-direction, a method based on that used by Fromang and Papaloizou (2006) is used, employing a cubic spline to bring the vertical gravity smoothly to zero between $|z| = z_{\rm change}/2$ and $|z| = z_{\rm change}$ where $z_{\rm change}$ is a new parameter introduced for this purpose:

$$g = \begin{cases} \Omega^2 z & \text{if } |z| < z_{\rm change}, \\ -8\Omega^2 z_{\rm change} + 20\Omega^2 z - \frac{14\Omega^2}{z_{\rm change}} z^2 + \frac{3\Omega^2}{z_{\rm change}^2} z^3 & \text{if } z_{\rm change} \leq |z| < 2z_{\rm change}, \\ 0 & \text{if } |z| \geq 2z_{\rm change}. \end{cases} \tag{2.24}$$

Using this prescription for the z-gravity component, and keeping z_{change} smaller than the scale height of the simulation box, but much larger than the scale height of the disk allows a standard outflow boundary condition to be additionally a hydrostatic boundary condition.

The vertical self-gravity and vertical external gravitational forces are treated with the FLASH `ppm_modify` coupling (Zingale et al., 2002), which assumes that the gravitational accelerations are locally balanced by a hydrostatic atmosphere. The x and y shearing frame forces from Hill's equations are cou-

pled though the FLASH frame geometry coupling, which uses the conventional PPM body force coupling.

2.4.3 Gravity-Hydrodynamics Coupling

In the case of an atmosphere supported in hydrostatic equilibrium against a gravitational force, it is important that the spurious accelerations from the inexact cancellation of the supporting pressure gradient and gravity force are minimized as these accelerations can build to significant velocities over many time steps. FLASH has implemented a technique proposed by Zingale et al. (2002) to partially handle this issue. In this approach, the pressure used for the left and right states of the PPM Riemann solver are corrected on the assumption that the gas is in equilibrium and the only pressure gradient available to generate waves is that which cannot be locally supporting the gas against gravity. Zingale et al. (2002) gives results for this technique with a constant gravitational acceleration and a variety of density profiles. In this work, it was found that this approach was problematic - spurious z velocities were generated, primarily at the mid-plane. To extend the work of Zingale et al. (2002) to systems like those studied in this work, an isothermal disk where the gravitational force changes with the z coordinate and has a sign change has been examined. The pair of functions which satisfy the hydrostatic equilibrium $dP(z)/dz = -(\rho g)(z)$ are:

$$P(z) = \frac{1}{2} H e^{-\frac{z^2}{H}}, \tag{2.25}$$

$$(\rho g)(z) = -g|z|e^{-\frac{z^2}{H}}. \tag{2.26}$$

Figure (2.4) follows the similar example in (Zingale et al., 2002) and plots the modified left and right pressure states used in the Riemann solver for this configuration. Ideally the left and right pressure states would be horizontal lines so that no wave would be generated at the interface. Where the monotonicity constraints of PPM interpolation are used, the corrected states are significantly in error, leading to spurious velocities. This error is inherently resolution dependent.

The method of Zingale et al. (2002) can be seen as an assumption that the Lagrangian frame in which the Riemann problem is solved is not accelerating with respect to the Eulerian frame. If the Zingale et al. (2002) method is used in a free-fall flow the modified pressures will instead introduce spurious velocities at each time step. This makes it clear that the root of this problem is that the Riemann problem, which depends on the left and right density, pressure, velocity and equation of state only, is not invariant between frames of different constant acceleration. Though various methods can be proposed to work around this limitation, it appears to be a fundamental property of all Godunov-type schemes.

2.4.4 Resolution Requirements from Gravity

Truelove et al. (1997) showed in isothermal self-gravitating gas simulations that in order to avoid spurious fragmentation of collapsing clouds it is necessary to have at every spatial location in the volume a grid spacing fine enough such that the local Jeans length is several times the local grid spacing. In the isothermal simulations in this thesis this criteria is satisfied by the selection of initial parameters. In simulations with cooling, the resolution de-

pendent temperature limiter of Wada and Norman (2007), as given in equation (2.22) is employed to ensure this criteria is satisfied, at the cost of preventing cooling past this point. This limiter limits the internal energy of each cell in such a way that the Jeans length is at least 1.5 grid cells. In this work, no significant fragmentation of cold lumps was seen, either physical or artificial. The fragmentation occurring in the simulations presented here occurred in gas well away from the temperature limits.

Similarly at large scales, Kim and Ostriker (2007) point out that in local models it is necessary to maintain a simulation box size L larger than a Jeans length – when a single Jeans length can be evaluated globally for the volume (i.e. when the gas is isothermal) Kim and Ostriker (2007) define a parameter n_J:

$$n_J = \frac{G\Sigma L}{c_s^2}, \tag{2.27}$$

which gives the number of Jeans lengths contained in the box length, where Σ is the surface density and c_s is the sound speed. This parameter should have a value greater than 1. This criteria is enforced by choosing the initial conditions appropriately in isothermal simulations.

As observed in Zingale et al. (2002), spurious velocities generated in the hydrostatic atmosphere will be related to the resolution of the grid versus the characteristic vertical scale (scale height) of the atmosphere. This limits the useful minimum resolution used in the upper regions of the disk.

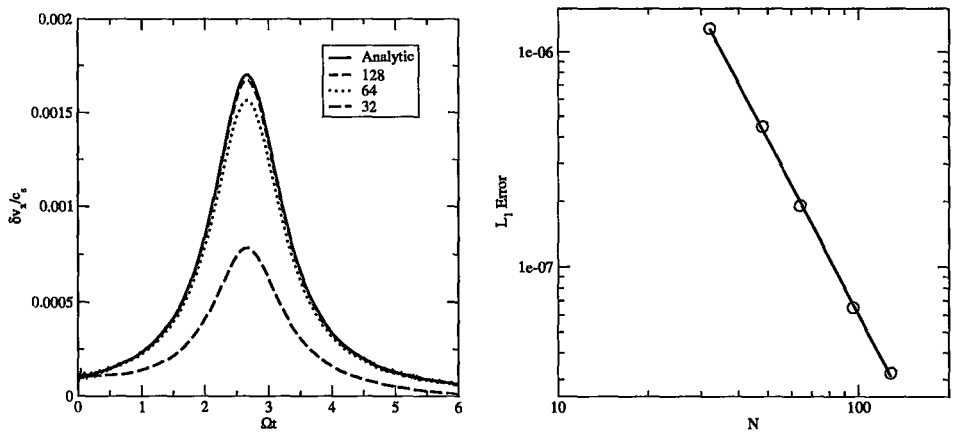

Figure 2.5: *Left:* Linear incompressible wave test evolution on grids of size $N^2 = 32, 64, 128$ *Right:* Convergence of L_1 norm error of maximum amplification, the index of the power law fit is -2.7

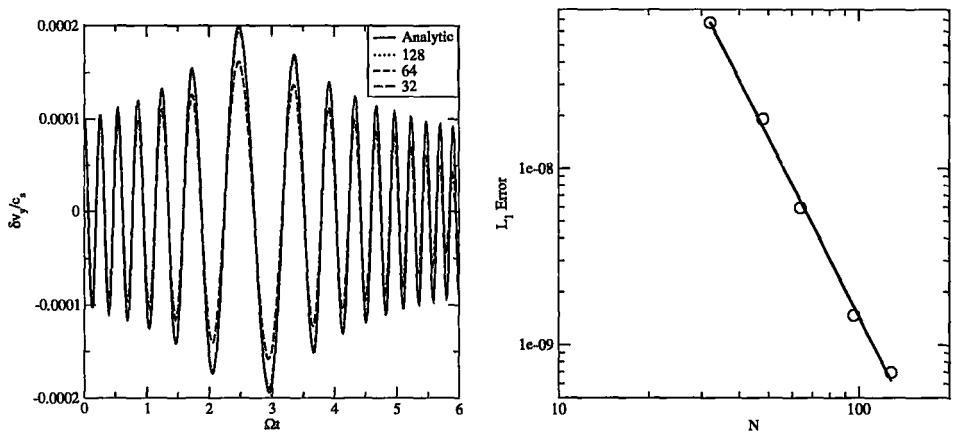

Figure 2.6: *Left:* Linear compressive wave test evolution on grids of size $N^2 = 32, 64, 128$ *Right:* Convergence of L_1 norm error of maximum amplification, the index of the power law fit is -3.4

2.5 Linear Wave Tests

To verify the correctness of the implementation used in this thesis of the shearing box boundary conditions, the evolution of linear velocity perturbations has been tested. Work by Johnson and Gammie (2005a) gives a solution for the evolution of incompressible and compressive plane waves in isothermal gas in the shearing box.

For these tests, shearing box parameter values of $q = \frac{3}{2}$ and $\Omega = c_s = 10^{-3}$ were used. Isothermal gas was approximated by using $\gamma = 1.00001$ in the equation of state.

A plane wave in the shearing box can be represented as

$$v_x = \delta v_x(t) \exp[ik_x(t)x + ik_y y] \tag{2.28}$$

$$v_y + q\Omega x = \delta v_y(t) \exp[ik_x(t)x + ik_y y]. \tag{2.29}$$

In general, for a plane wave with wave vector $\mathbf{k} = k_x\hat{x} + k_y\hat{y}$ the wave will shear as the background flow, that is $k_x(t) = k_{x,0} + q\Omega k_y t$.

For an incompressible (vortical; $\nabla \cdot \mathbf{v} = 0$) wave the evolution of the velocity amplitude is given by:

$$\delta v_{xi} = \delta v_{xi0} \frac{k_0^2}{k^2} \tag{2.30}$$

This evolution has been used as a test case in (Johnson and Gammie, 2005b) and (Shen et al., 2006). The initial wave vector used was:

$$k_{x,0} = -8\left(\frac{2\pi}{L_x}\right), \qquad k_y = 2\left(\frac{2\pi}{L_y}\right). \tag{2.31}$$

To satisfy the requirements of being a small perturbation and giving an incompressible wave the initial velocity amplitudes were chosen as:

$$\delta v_{x,0} = 10^{-4} c_s, \qquad \delta v_{y,0} = 4 \times 10^{-4} c_s. \tag{2.32}$$

Figure (2.5) shows the convergence of the solution in this linear incompressible wave test has also been computed by Johnson and Gammie (2005b) and Shen et al. (2006).

The case of a linear amplitude compressible wave ($\nabla \cdot \mathbf{v} \neq 0$) has been presented as a test case by Johnson and Gammie (2005b) and Shen et al. (Shen et al., 2006) and this test has been repeated with the code described in this thesis. The analytic solution is given by Johnson and Gammie (2005a) as

$$\ddot{\delta} v_{yc} + \left(c_s^2 k^2 + \kappa^2\right) \delta v_{yc} = 0. \tag{2.33}$$

Using a time scaling

$$T \equiv i\sqrt{\frac{2c_s k_y}{q\Omega}} \left(q\Omega t + \frac{k_{x0}}{k_y}\right) \equiv i\sqrt{\frac{2c_s k_y}{q\Omega}} \tau \tag{2.34}$$

and defining the non-dimensional constant C

$$C \equiv \frac{c_s^2 k_y^2 + \kappa^2}{2q\Omega c_s k_y} \tag{2.35}$$

this evolution equation can be rewritten as

$$\frac{d^2 \delta v_{yc}}{dT^2} + \left(\frac{1}{4} T^2 - C\right) \delta v_{yc} = 0. \tag{2.36}$$

This is a parabolic cylinder equation (Abramowitz and Stegun, 1964, §19). The wave vector is defined by $k^2 \equiv k_x^2 + k_y^2$ and the epicyclic frequency is $\kappa^2 \equiv (2-q)\Omega^2$. The solution to equation (2.36) can be expressed in terms of the associated parabolic cylinder functions. In practice, the solution is expressed in terms of linear combinations of the Maple implementation of these functions

$$\Re\left(\texttt{CylinderU}(-iC, Te^{1/4i\pi})\right) \tag{2.37}$$

and

$$\Re\left(\texttt{CylinderV}(-iC, Te^{1/4i\pi})\right). \tag{2.38}$$

For the case used to test the code described in this thesis, the initial wave vector was

$$k_{x,0} = -4\left(\frac{2\pi}{L_x}\right), \qquad k_y = \frac{2\pi}{L_y}, \tag{2.39}$$

and to make the wave irrotational the initial velocity amplitude was chosen as

$$\delta v_{x,0} = -4 \times 10^{-4} c_s, \qquad \delta v_{y,0} = 10^{-4} c_s. \tag{2.40}$$

Figure (2.6) shows the linear compressible wave test convergence.

2.6 Initial Conditions

As the form of the gravitational potential is complicated (a fixed background potential plus a periodic solution to Poisson's equation) attempting to write an analytic form for the initial isothermal hydrostatic equilibrium configuration has been avoided. Instead, to create an isothermal hydrostatic initial conditions a simulation was run with the same vertical grid configuration as the

full simulation but with minimal horizontal extent, only z-direction hydrodynamics and fully periodic boundary conditions. To encourage the relaxation of the gas, the cooling operator was modified to remove 20% of the cell's momentum at each step. This simulation was started with the desired smooth surface density of gas, and evolved until an equilibrium configuration is attained. A vertical profile was extracted from this result, and exactly replicated as the initial condition for the full simulation.

Additionally, non-isothermal hydrostatic initial conditions have been created with this method. For example an initial condition everywhere satisfying the heating-cooling equilibrium in the warm, thermally stable $6102 - 10^5$ K regime has been created by running the same simulation with a cooling operator which extends the slope from this regime to all temperatures. Since this is a thermally stable regime, for viable surface densities the gas relaxes to a hydrostatic equilibrium satisfying the heating-cooling equilibrium of the full cooling operator.

This technique of relaxing to the initial condition has the added advantage that the result is as close as possible to a numerical representation of the hydrostatic equilibrium, not an analytical version.

2.7 Methods of Perturbing Initial Conditions

In order to seed instability in the system in a controlled and repeatable manner, it is necessary to perturb the otherwise stable initial conditions. This perturbation should be larger than any numerical perturbations present. Two methods have been used. First, irrotational velocity perturbations have been used in some simulations. These have a Kolmogorov-like power spectrum $k^{-\frac{5}{3}}$

in modes with $k_z = 0$ and k_x, k_y one of $2, 4, 8$ only. This restriction is used to ensure that the perturbed initial condition has zero linear momentum. Second, in a manner similar to Wada and Norman (2007) and Pinotek and Ostriker (2007) random (uniform distribution) density perturbations with maximum amplitude 1% of density have been used in some simulations. In the case of simulations with cooling, these density perturbations are a more minimal assumption than velocity perturbations, and are consistent with earlier work.

2.8 Summary of Methods

As described in this chapter, a parallel shearing box has been implementation, with specific modifications to improve performance with thermal instability has been written and tested for correctness. In the z-direction, an appropriate mixed boundary condition for gasdynamics, external gravity and self-gravity has been implemented. Finally, a method for solving for a hydrostatic atmosphere in the combined external gravity and self-gravity on an adapted mesh has been devised. This framework can be used to efficiently run simulations of galactic gas disks. For example, on 8 processors of the Sharcnet cluster Bala (Opteron 2.20 GHz, Myrinet G2) the simulation of §3.3 labeled A1 took 605161 s for 5824 time steps, with 60% of the time spent on gravity and 33% on gasdynamics.

Chapter 3

Results

The core issue in understanding the role that self-gravity and thermal instability can have in driving turbulent motions in an extended galactic disk is in how these mechanisms can lead to the transfer of angular momentum. The importance of this is that it allows the transport of mass inwards and so liberates energy from the rotational motion of the galaxy with which turbulent motions can be driven. The physical structures which arise, or fail to arise, in the disk to allow the coupling between self-gravity and angular momentum transport are a primary concern. To probe this three sets of simulations were run using the methods described in §2. The first evolved a perturbed isothermal disk with $Q \approx 1$. The second consisted of a fixed surface density disk with cooling enabled, in a similar manner to Wada and Norman (2007) and Pinotek and Ostriker (2007). Finally, the third set of simulations involved a disk continuously accreting mass, so that a phase transition occurs suddenly during the evolution.

Table 3.1: Parameters of Isothermal Simulations

Name	Q	n_j	Mid-plane Resolution
I1	1.16	4.61	128^2
I2	1.16	4.61	256^2

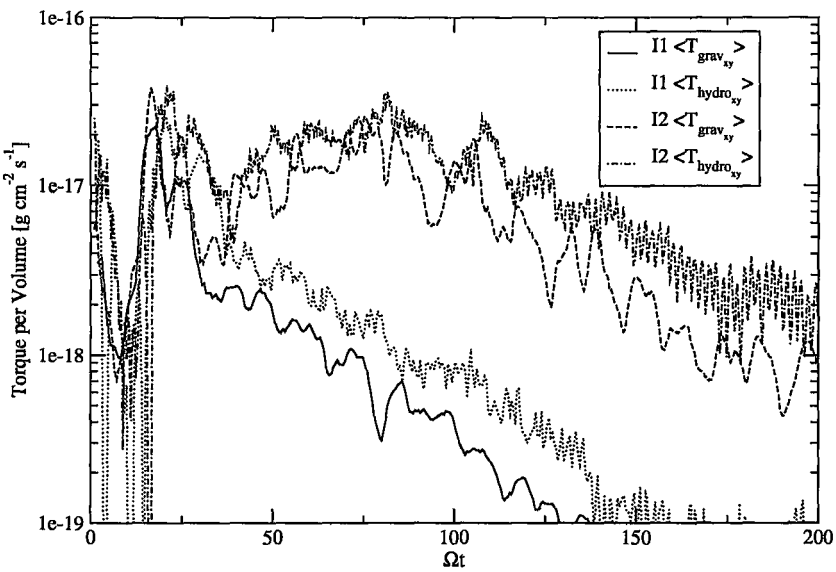

Figure 3.1: Stress in isothermal disk runs I1 and I2. This is sampled every 50 cycles, averaged over 10 samples for readability.

3.1 Isothermal Runs

To evaluate the action of only self gravity, without thermal instability, in driving turbulence in a local patch of a galactic disk, isothermal gas can be used. Isothermal runs have a particular importance that Q is only well-defined in this case, in that there is no ambiguity in needing to define an average value of Q. Table (3.1) lists the runs. The Q value of 1.16 was selected as being a value marginally stable against fragmentation by axisymmetric perturbations, and hence the most likely to form a gravitoturbulent quasi-steady state. The number of runs used in this section was minimal, due to the resources required to evolve the calculation at the higher resolution for a sufficiently long time. All runs use an 8×10^{21} cm by 8×10^{21} cm by 16×10^{21} cm simulation box. The base grid is 2 by 2 by 4 blocks of 8 by 8 by 8 cells, with a minimum of 2 levels of refinement everywhere. Run I1 has 4 levels of refinement on the mid-plane or 128^2 resolution and run I2 has 5 levels of refinement on the mid-plane or 256^2 resolution. The z_{change} parameter is 4×10^{-21} cm. Velocity perturbations as described in §2.7 were used with a maximum velocity 42% of the sound speed. The evolution of the angular momentum transporting stress (see §1.1.5) for runs I1 and I2 is shown in figure (3.1). These simulations decay towards a steady state that is a smooth hydrostatic flow without significant angular momentum transport. The decay of the stresses indicates that no gravitoturbulent quasi-steady state was found.

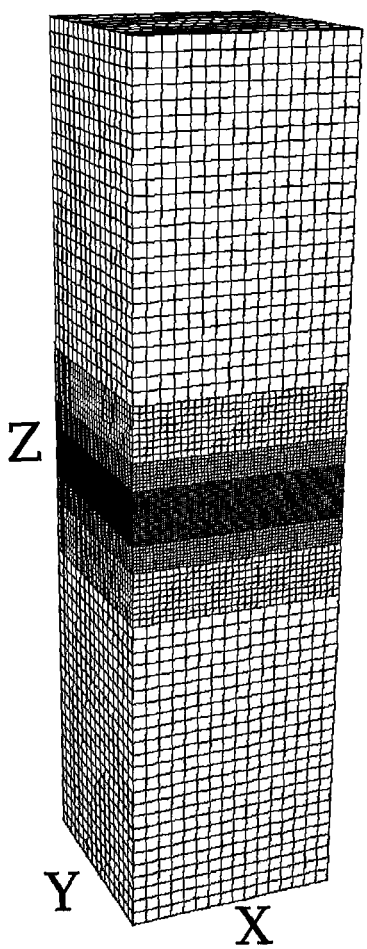

Figure 3.2: Grid configuration from run C1.

Table 3.2: Parameters of Cooling Simulations

Run Label	Σ [$M_\odot$ pc^{-2}]	T_0 [K]	Vertical Pattern	Initial Maximum Density [g cm^{-3}]
C6	1.5	100	single-phase	1.401×10^{-24}
C5	1.5	2500	single-phase	2.809×10^{-25}
C4	1.5	10000	single-phase	1.001×10^{-25}
C1	6	2500	two-phase	1.040×10^{-24}
C2	6	2500	two-phase	1.030×10^{-24}
C7	6	10000	single-phase	4.405×10^{-25}
C3	15	10000	two-phase	1.342×10^{-24}

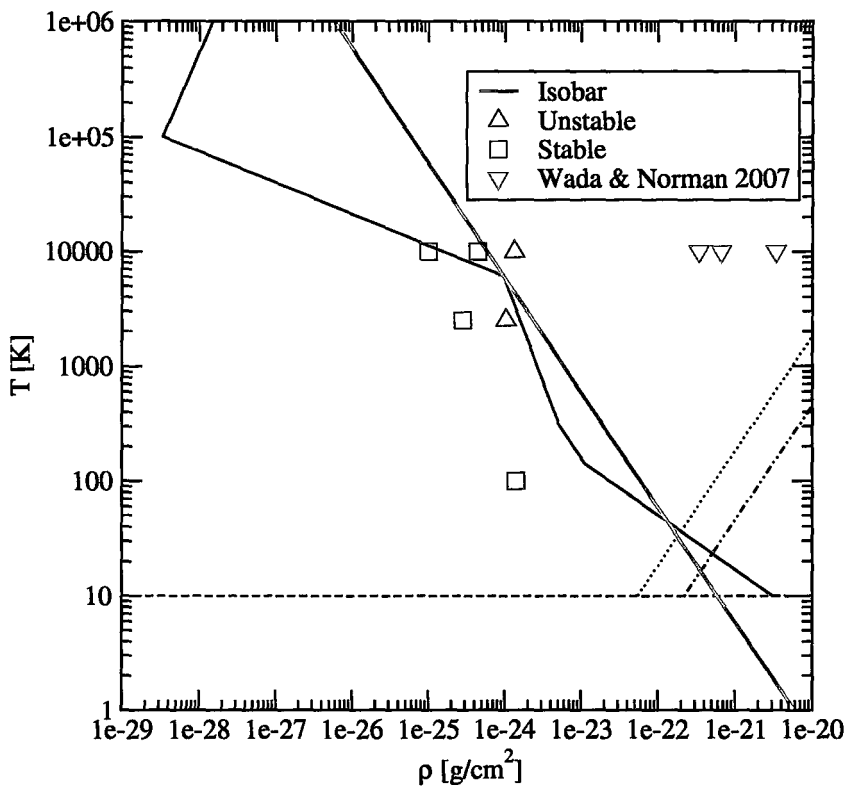

Figure 3.3: Maximum density of initial conditions and their evolution in relation to the curves from figure (2.3). The symbols corresponding to runs C1 and C2 lie directly on top of each other.

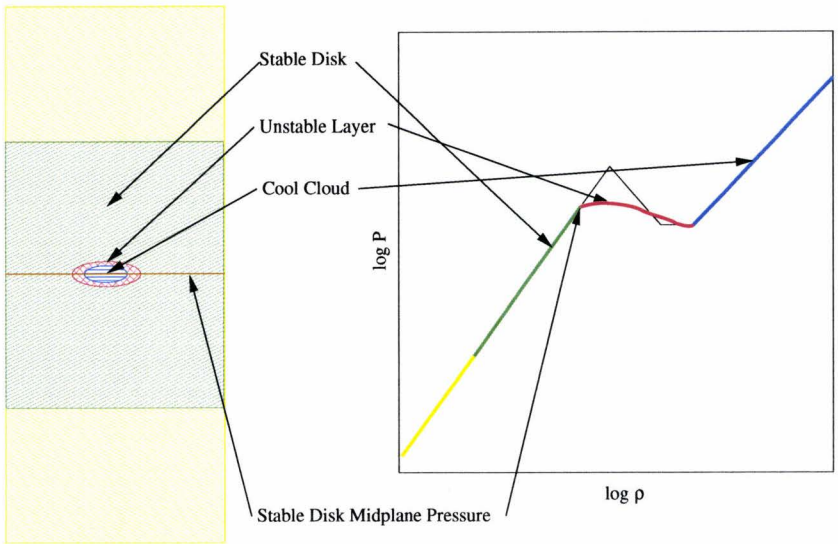

Figure 3.4: Schematic of structure of a two-phase disk. The thin line denotes the equilibrium solution and the thick lines denote the spread of each gas component.

3.2 Runs with Cooling

As runs with an isothermal equation of state have produced no significant activity, the cooling operator was enabled in another set of simulations. The basic parameters of these runs including cooling are a box 1.2 kpc by 1.2 kpc by 4.8 kpc, with a base grid of 2 by 2 by 4 blocks of 8 by 8 by 8 cells with no minimum level of refinement, as illustrated in figure (3.2). All cooling runs except C2 use 4 levels of refinement at the mid-plane or a mid-plane resolution of 128^2 and 9.375 pc. Run C2 uses 5 levels of refinement at the mid-plane, or a mid-plane resolution of 256^2 and 4.6875 pc. Table (3.2) lists the basic parameters of each run. The initial condition was an isothermal disk, with 1% evenly distributed random density perturbations added to each cell.

There are two basic fates which these simulations have, one is where the disk remains as one phase and the perturbations die out, the second is for two

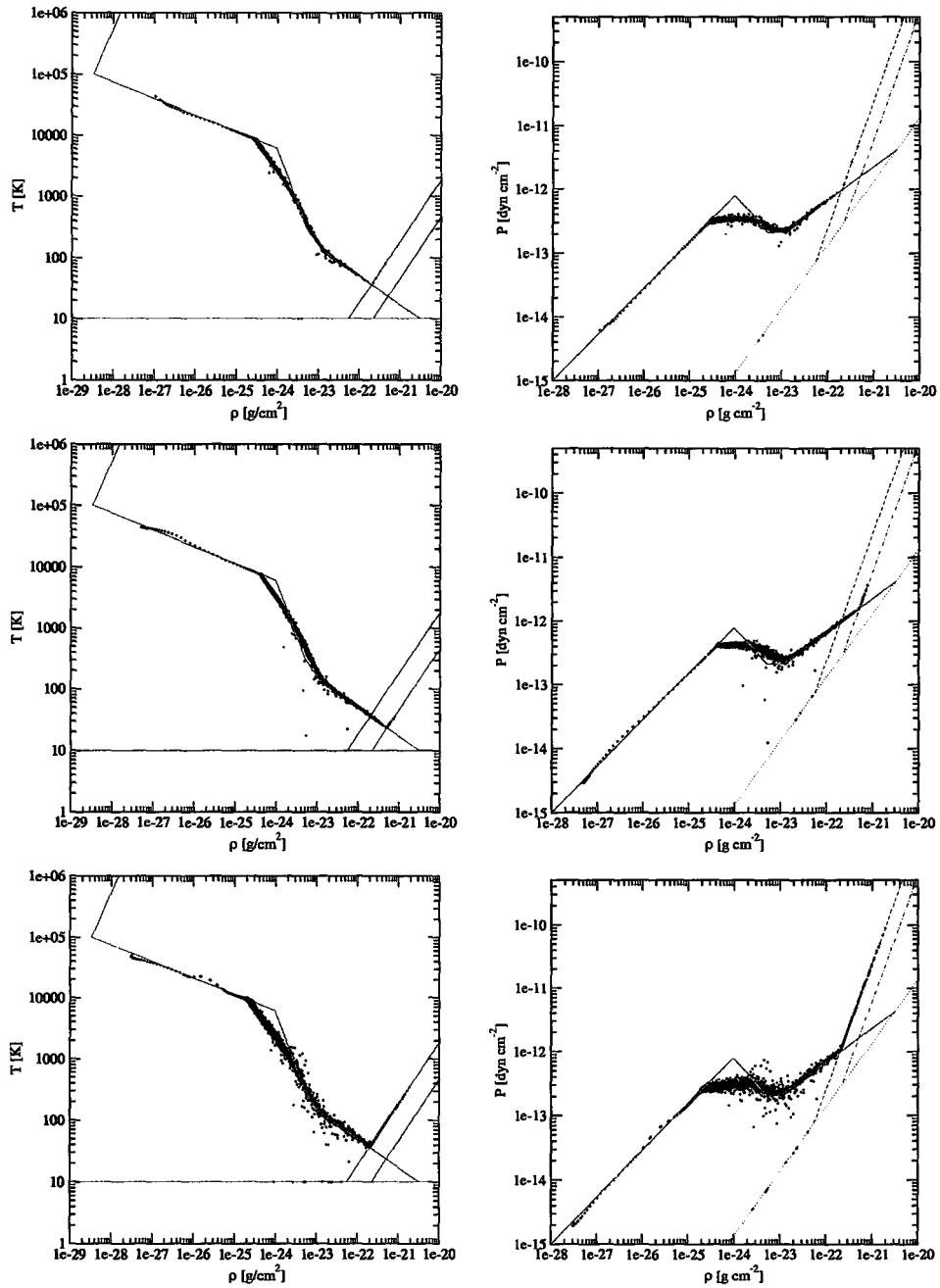

Figure 3.5: Phase plots of runs ending in a fragmented two-phase disk. *Left:* In temperature v.s. density *Right:* In presssure v.s. density, from top to bottom, runs C1, C2 and C3. These taken at time $t = 1.19 \times 10^{16}$ s, $t = 5.82 \times 10^{15}$ s, $t = 3.50 \times 10^{15}$ s respectively.

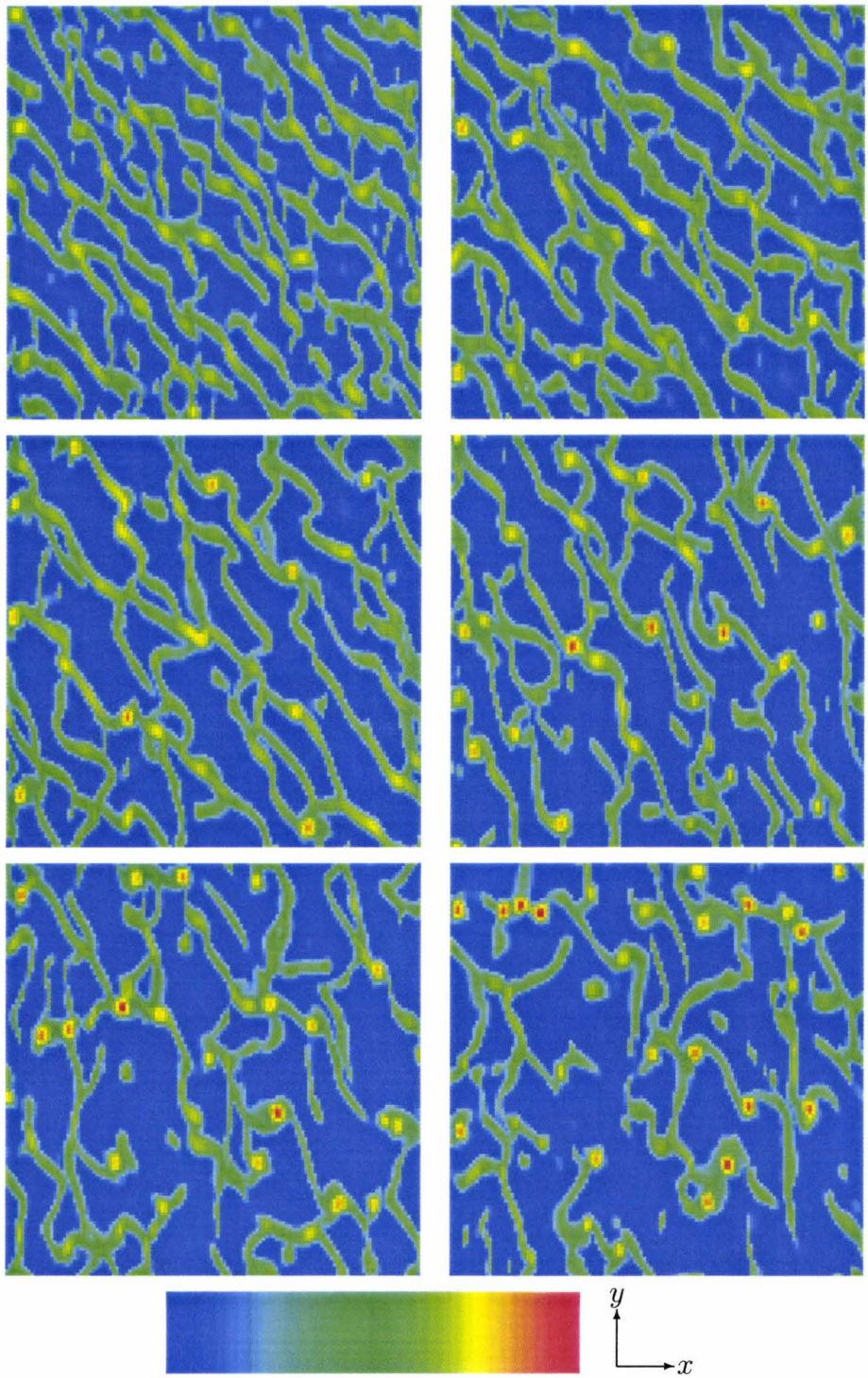

Figure 3.6: Run C1 density slice at mid-plane. The density scale is logarithmic, ranging from blue 2.838×10^{-25} g cm^{-2} to red 1.302×10^{-21} g cm^{-2}, at times $t = 6,7,8,9,10,11 \times 10^{16}$ s. The simulation box is 1.2 kpc wide.

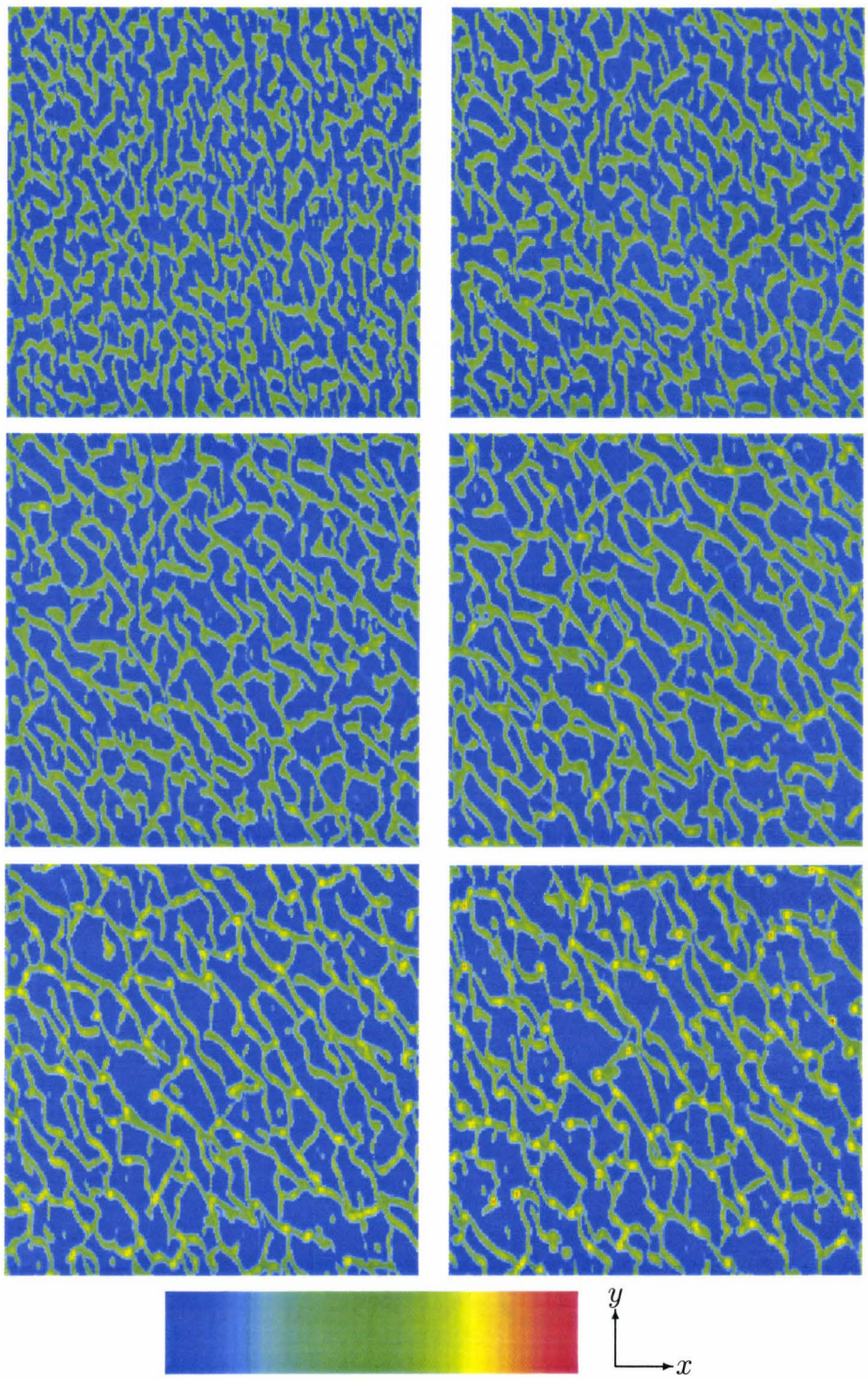

Figure 3.7: Run C2 density slices at mid-plane The density scale is logarithmic, ranging from blue 3.726×10^{-25} g cm^{-2} to red 2.676×10^{-21} g cm^{-2}, at times $t = 3.0, 3.5, 4.0, 4.5, 5.0, 5.5 \times 10^{15}$ s. The simulation box is 1.2 kpc wide.

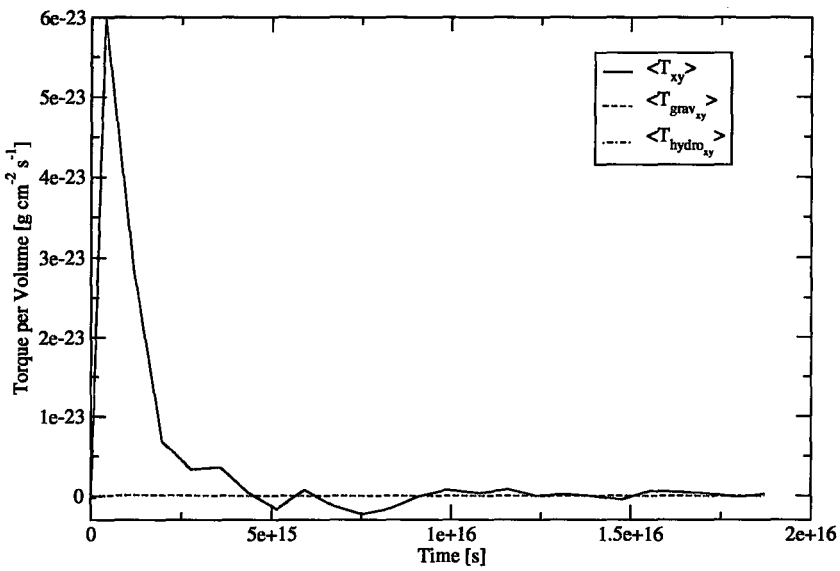

Figure 3.8: Run C7 stress – showing stable disk

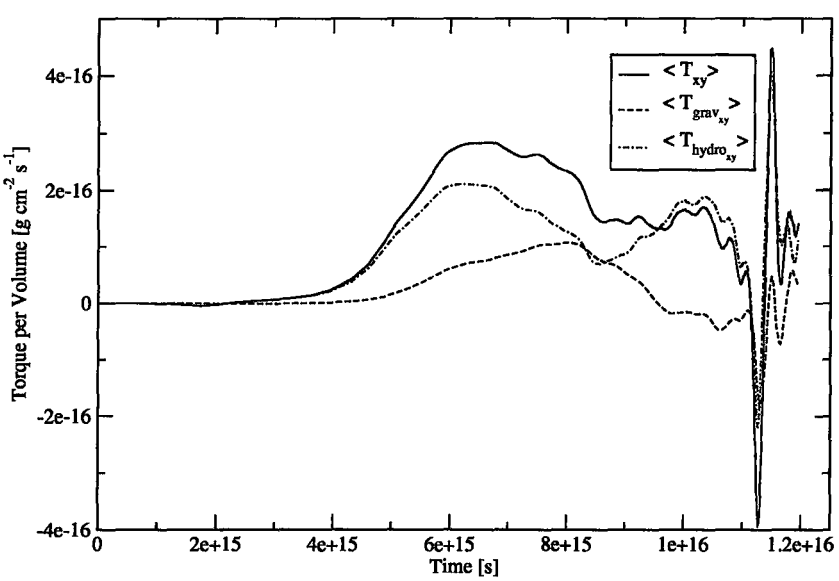

Figure 3.9: Run C1 stress – an unstable case

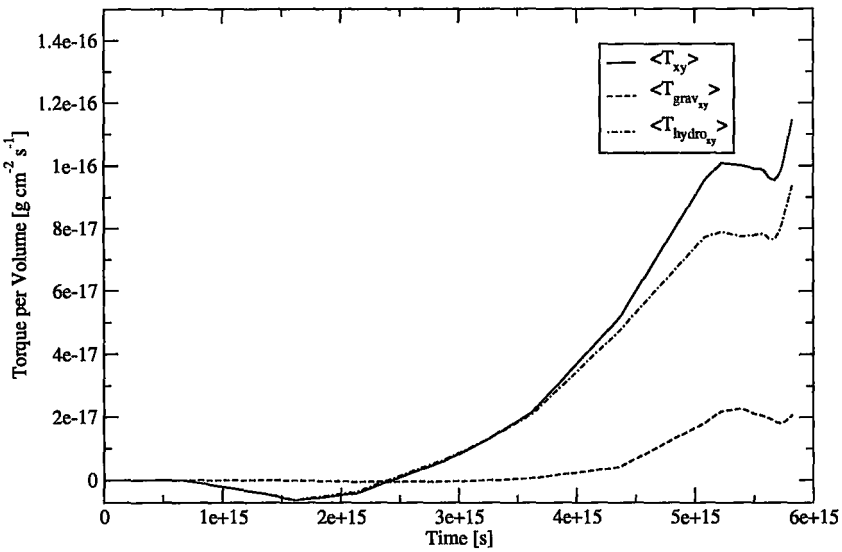

Figure 3.10: Run C2 stress – an unstable case

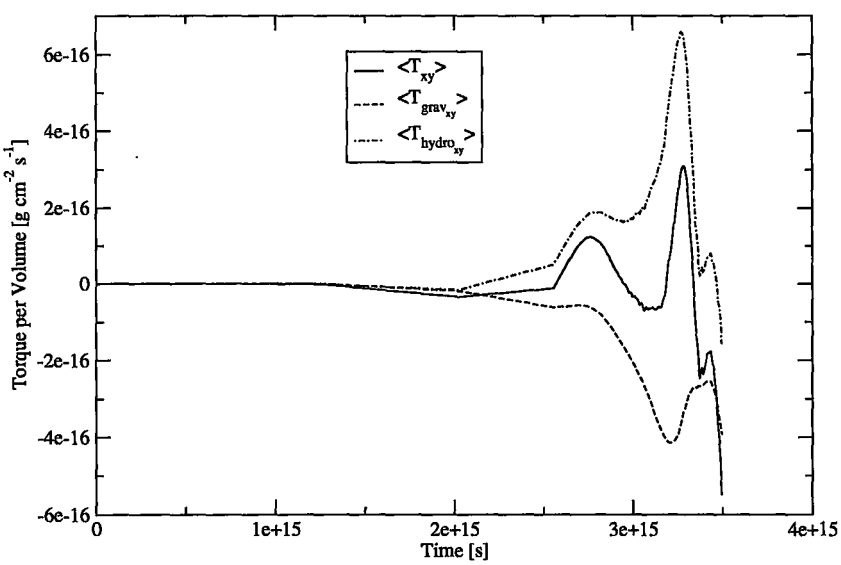

Figure 3.11: Run C3 stress – an unstable case

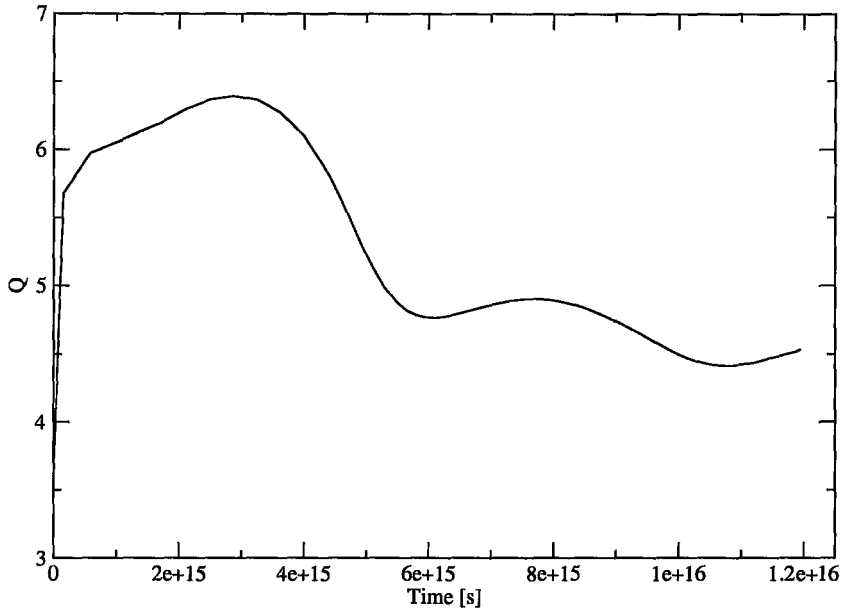

Figure 3.12: Run C1 $\langle Q \rangle_\rho$

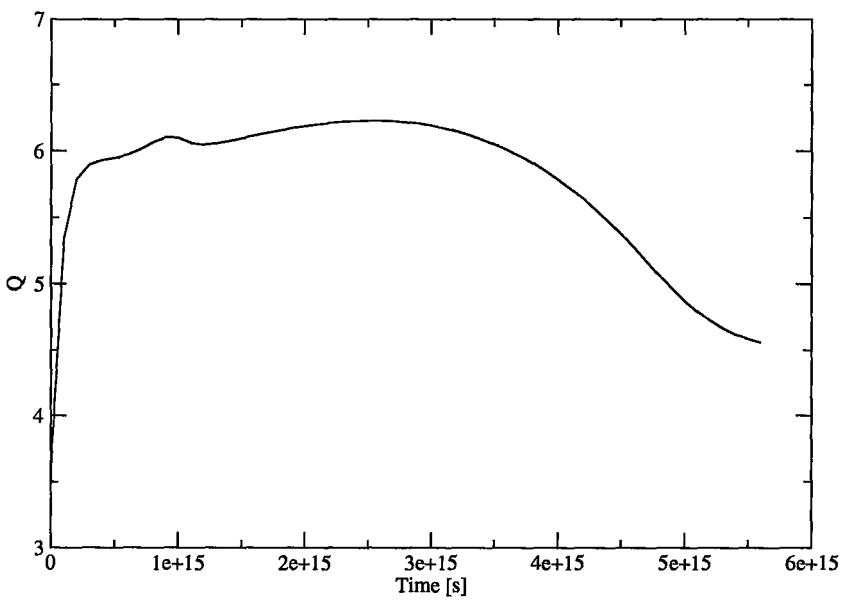

Figure 3.13: Run C2 $\langle Q \rangle_\rho$

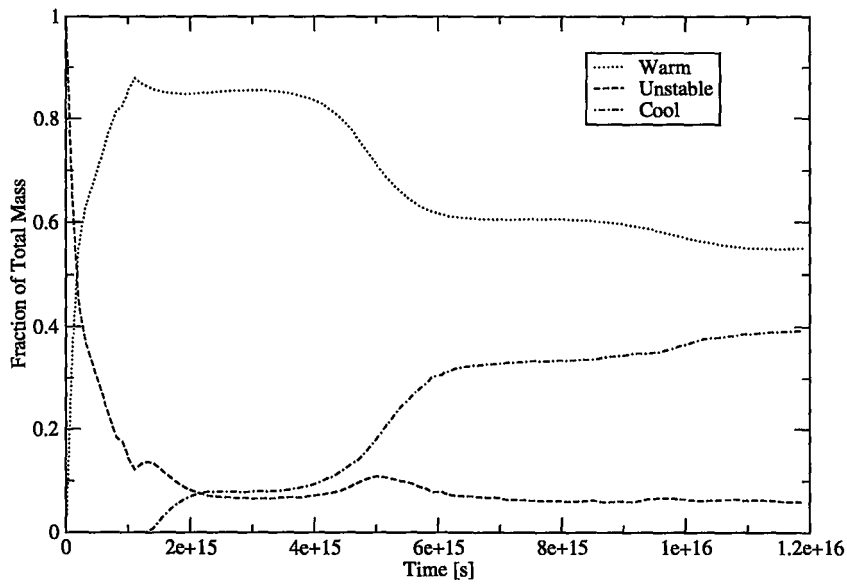

Figure 3.14: Run C1 fractions of warm, cool and unstable gas over time

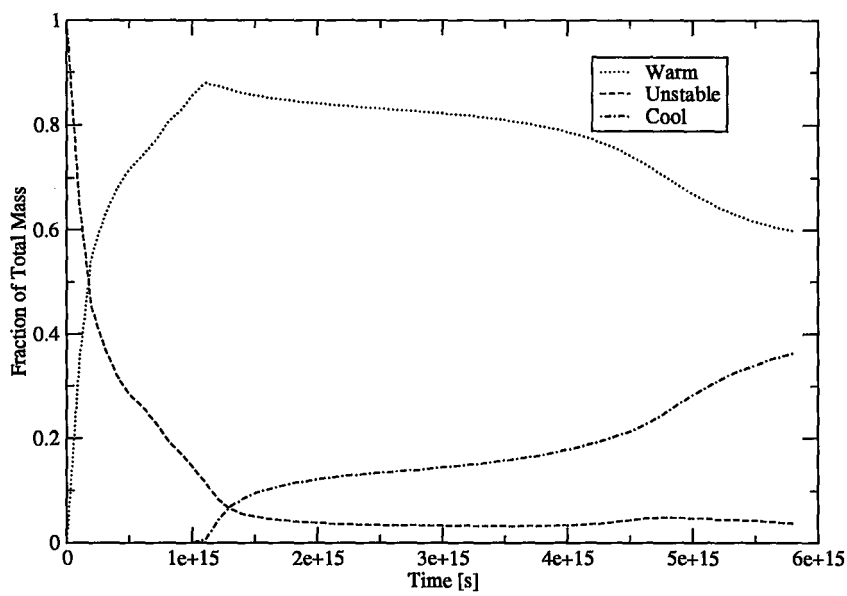

Figure 3.15: Run C2 fractions of warm, cool and unstable gas over time

phases to form and the perturbations grow. Figure (3.3) shows a phase plot of the initial conditions indicating the maximum density and the ultimate fate. Plotted are the equilibrium and temperature limit curves as in figure (2.3), an example isobar associated with the pressure at which thermal instability becomes active on the equilibrium curve and the maximum density of each initial condition in table (3.2), coded by the ultimate fate of the simulation. If plotted, the gas for each initial condition would extend in a horizontal line from the maximum density marker past the left boundary of the plot. This figure also shows the initial conditions used by Wada and Norman (2007) for comparison these are far to the unstable side of the space. When a two-phase disc forms its configuration can be characterized by the cartoon representation in figure (3.4). The dense lumps compress, accrete mass, and coalesce after they form. The unstable filaments connecting the lumps are gradually accreted into clouds and an unstable layer exists as a sheath around the cool clouds. A Q-stable disk of thermally stable gas remains extending far above the clouds. The phase diagram of this two-phase medium for two different resolutions and surface densities is displayed in figure (3.5). It is notable that the distribution of points follows the equilibrium solution and Jeans limiter lines closely, except for a region where the points progress in a manner closer to an isobaric solution between the two thermally stable sections of the equilibrium curve.

As can be seen by comparing the evolution in the mid-plane density slices in figure (3.6) and figure (3.7) the scale at which filaments develop varies significantly between the two resolutions. Roughly, the scale on which the fragmentation happens is smaller when smaller scales are resolved in the simulation. This suggests that the mechanism for generating fragmentation is not spatially resolved in these simulations. Of the two scales where instabilities

act most strongly in these simulations, the numerical Field length is related to the grid resolution, whereas the Jeans length is always resolved.[1] Additionally, the numerical method used in this thesis does not explicitly determine or control the numerical Field length. Hence, it is likely that the Field length is important to the scale of the fragmentation.

The phase structure of the disk in these simulations has distinct consequences for the transport of angular momentum, and hence the possibility of extracting energy from differential rotation of the galaxy. For a stable case, shown in figure (3.8), the stress decays quickly, mirroring the fate of the isothermal disk of the previous section. For cases where a two-phase disk forms, figures (3.9), (3.10) and (3.11) show that the fragmentation of the cool phase leads to much larger values for the angular momentum transporting stress $\langle T_{xy} \rangle$. In addition, the fragmentation of the cool phase does not necessarily imply that the global mass weighted average Q ($\langle Q \rangle_\rho$) must be < 1. As shown in figures (3.12) and (3.13), Q can be still in the range associated with stability, even though parts of the disk are violently unstable.

For the times where they overlap, runs C1 and C2 show similar evolution of the fraction of total mass in each temperature range, as shown in figures (3.14) and (3.15). That the cool gas mass is constantly increasing indicates that a quasi-steady state has not been achieved – more gas is cooling than is reheated by gas motions.

Reliable velocity dispersion measurements cannot be inferred from these simulations. As the gas initially heats strongly from the isothermal initial condition, the disk scale height initially climbs rapidly before falling as the mid-

[1]Infact the gas, during initial stages of the fragmentation, lies far in the phase diagram from even the Jeans Length limit.

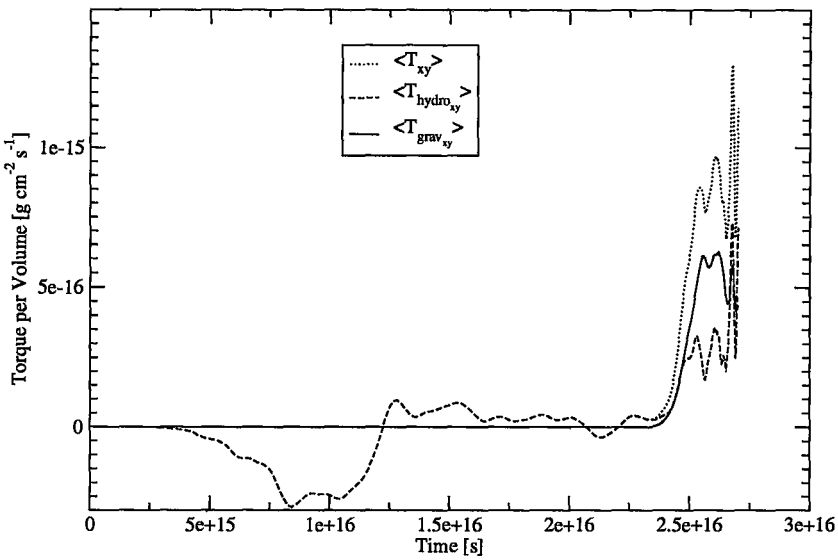

Figure 3.16: Run A1 stress – showing the transition from stable to unstable evolution

plane region cools and collapses. Through the rest of the simulation the disk oscillates slightly and thus dominates the density weighted vertical velocity dispersion. Hence, the existence of a stress by which velocity dispersion can be driven must be used as the indicator of a viable mechanism here.

3.3 Accreting Disk

From the previous section, it is apparent that the transition from a single phase disk to a two-phase disk is very important in determining how angular momentum can be transported though local self-gravitational stresses. To investigate this, a simple model of a accreting disk has been developed.

Run A1 starts with the grid as in run C2, but with an initial condition of uniform very low density (10^{-28} g cm^{-3}) gas. Then, instead of outflow z direction boundaries as in run C2, inflow boundaries are specified by setting

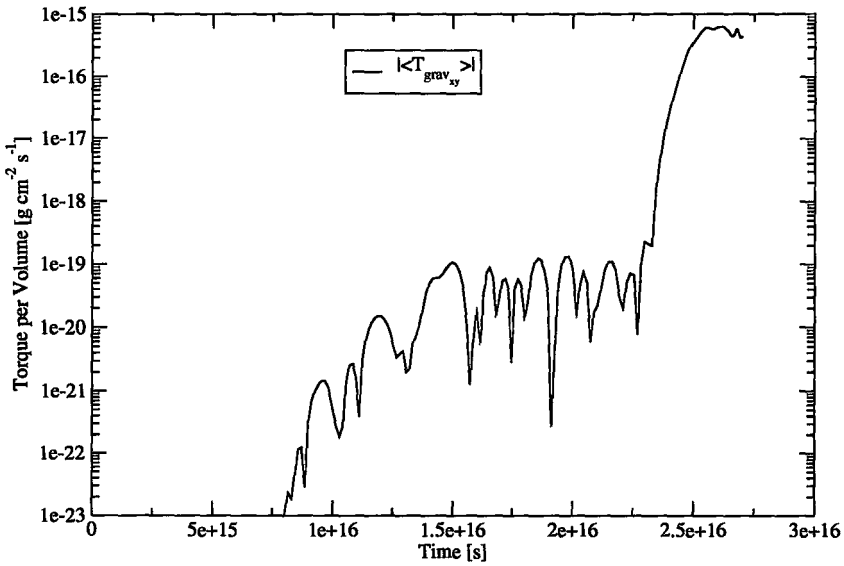

Figure 3.17: Run A1 absolute value of gravitational stress

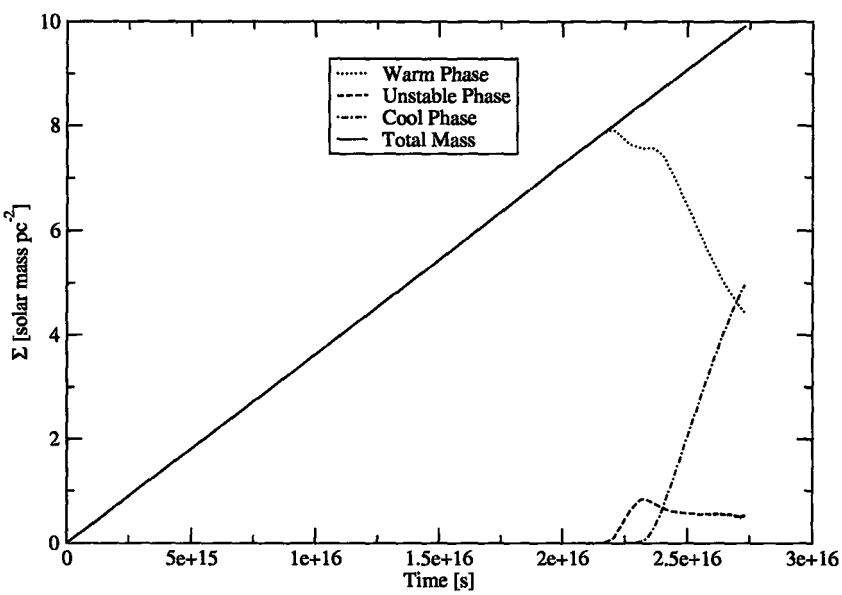

Figure 3.18: Run A1 mass fraction by phase

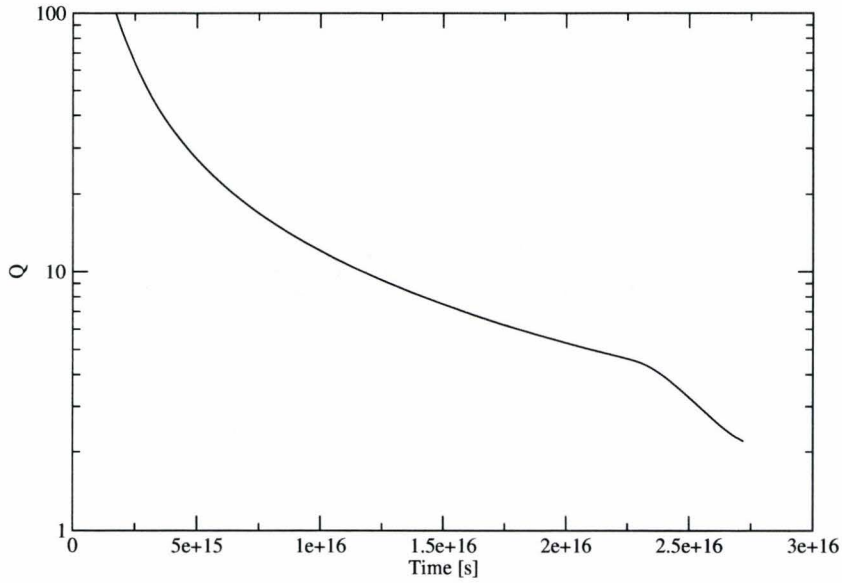

Figure 3.19: Run A1 $\langle Q \rangle_\rho$

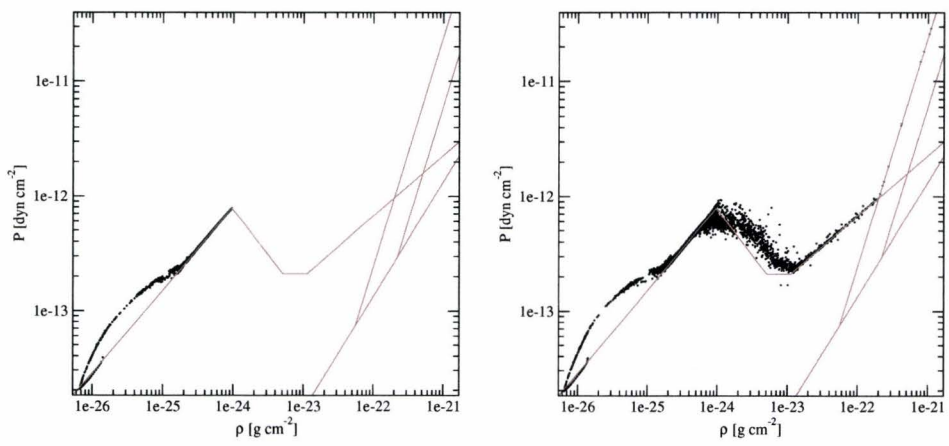

Figure 3.20: Phase plots of run A1 *Left:* At time $t = 2.13 \times 10^{16}$ s *Right:* At time $t = 2.73 \times 10^{16}$ s

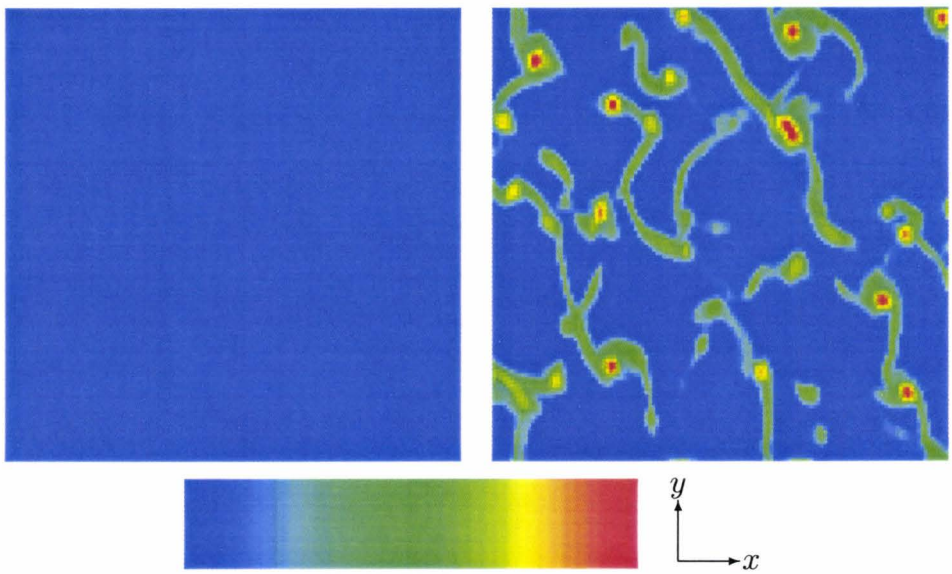

Figure 3.21: Mid-plane density slice plots of run A1. Density is plotted on logarithmic scale, from blue 4.61×10^{-25} g cm^{-2} to red 3.26×10^{-21} g cm^{-2}. The simulation box is 1.2 kpc wide. *Left:* At time $t = 2.07 \times 10^{16}$ s *Right:* At time $t = 2.72 \times 10^{16}$ s

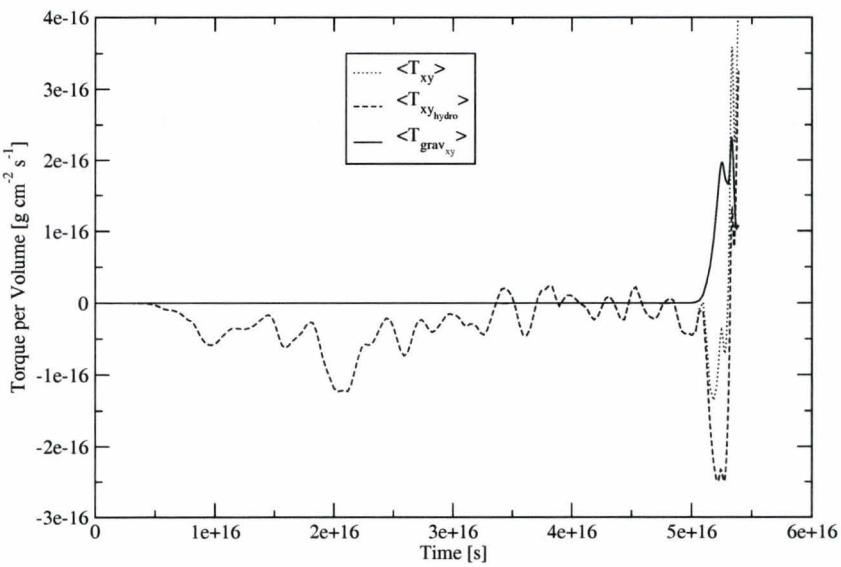

Figure 3.22: Run A2 stress

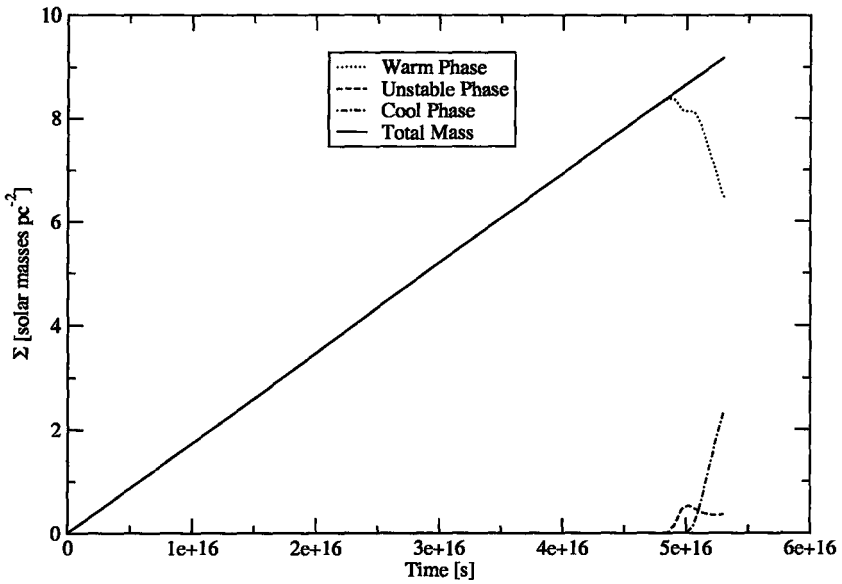

Figure 3.23: Run A2 mass fraction by phase

the gas density at 3.4815×10^{-26} g cm^{-3} and pressure at 4.5×10^{-15} dyn cm^{-2}. Along the 16 by 16 grid of cells at the z boundary, the density is 1% greater on odd-numbered rows. This provides a minimal, but non-angular momentum transporting perturbation to the flow, so that the imposed perturbations will be larger than those arising from purely numerical effects. The inflow rate was 1.146×10^{-8} M$_\odot$ pc^{-2} yr. With these boundary conditions, the disk built up and eventually reached the critical temperature/pressure for thermal instability and formed a cool phase with vastly enhanced angular momentum transport.

The evolution of angular momentum transporting stress is shown in figure (3.16). The gravitational torque $\langle T_{grav_{xy}} \rangle$ shows a rapid increase after a thermally unstable component of the disk develops. That the Rayleigh stress $\langle T_{hydro_{xy}} \rangle$ is of significant size before the phase change is due to the motions driven in the gas by the accretion, and is a direct result of the boundary

conditions. Figure (3.17), displaying the absolute value of the gravitational stress, shows an increase of approximately 4 orders of magnitude as a result of the development of the cool phase. It is important to note however that the pre-transition value of the gravitational stress is a result of the pre-transition density perturbations, which in turn are purely a function of the boundary conditions. However, taking the results of §3.2 into account, it can be stated that these pre-transition perturbations will not grow on their own. When the cool phase forms, mass is rapidly accreted into the cool clouds, as can be seen in figure (3.18). Like in the star formation cutoff theory of Elmegreen and Parravano (1994), Q shows a marked decline when the cool phase forms, as shown in figure (3.19). The value of this overall average Q is not simple to interpret, as the cool component has a much smaller sound speed and is highly fragmented. Scatter plots of the gas state just before and after the development of the cool phase in figure (3.20) show the transition from a single phase to a two-phase medium of a thick disk and cool clouds, as found in the simulations of §3.2. There is a notable difference between figures (3.20) and (3.5) in the position of the warm component points. In figure (3.20) the gas at the upper boundary sits on the equilibrium line, then as it falls in it becomes less dense and cools, until it begins running into the disk, compressing and rising off the equilibrium line. Most notably, as the gas becomes more dense, components cover the equilibrium line right to the maximum, not stopping where the bulk of the points progress right to the cool component line like in figure (3.5). The development of the cool clouds out of small pre-transition density perturbations is shown by the mid-plane density sliced in figure (3.21), where the later slice is reassuringly qualitatively similar to those in §3.2.

As a simple test of the sensitivity of the system to the boundary con-

ditions, the simulation A2 was run with an inflow rate of half of that used in A1. The evolution of the gravitational stress in run A2 shows the same effect from the phase transition as in run A1 (see figure (3.22)). The hydrodynamic and gravitational stresses in run A2 are of opposite sign when the growth due to the phase transition happens, unlike in run A1. The sign of the stress at this time is a result of the geometric configuration of the regions where the cool gas develops. The development of the mass fractions is shown in figure (3.23). The cold phase can be seen to develop at slightly higher surface density than in run A1 as would be expected due to the smaller confining pressure on the disk coming from the inflow. The difference in the evolution of stresses between A1 and A2 serve to illustrate that the particular path followed by each is not indicative of a typical evolution, only particular features connected to some physical changes are. These features are the change in the stresses following the phase change, and the pre-transition hydrodynamic stress due to the forcing of the disk by the inflow.

3.4 Discussion

The shearing box, due to the low order expansion used in its construction, does not specify which direction is radially inwards: the equations are perfectly symmetrical in the radial direction. Hence, although the large scale evolution of the system to lower energies dictates that angular momentum must be transported outwards, the local representation in the shearing box can momentarily transport angular momentum in either direction. This causes the stress to momentarily fluctuate in sign in some cases. Additionally, the local nature of the simulations means that the stress is created by the interaction

of a small number of dense clouds. This small number of interacting bodies further causes the calculated stress to fluctuate more than a large number of bodies would.

To review of the most basic property of the three sets of simulations presented here: the isothermal disk models tested did not sustain a quasi-steady gravitoturbulent state, the thermally stable cooling disks of fixed surface density decayed towards an smooth flow state and before the onset of thermal instability, the accreting disk models did not have significant gravitational stress. This suggests that a thermally stable galactic disk does not have the ability to drive turbulent motions through differential rotation and angular momentum transport by gravitational stresses or a gravitoturbulent quasi-steady state.

The results of §3.2 and §3.3 show that thermal instability and the formation of a two-phase medium can provide a mechanism for producing enhanced angular momentum transport by self-gravitational stresses. This will have two consequences: to convert the galaxy's rotational energy into local motions giving rise to velocity dispersion in the gas; and to enhance the rate at which mass, primarily in the form of cool gas clouds, is transported inwards enhancing the surface density of more central regions of the galactic disk. Increased surface density may lead to star formation.

No simulations shown in the thesis provide any examples of a gravitoturbulent quasi-steady state as found in Gammie (2001) – either they evolve towards a smooth steady state, or continue to fragment for all time without reheating cool gas.

The divide between stable and unstable initial conditions in §3.2 cannot be interpreted too strongly for a number of reasons. Since the thermal

instability is so important in the initial evolution, the precise form and normalization of the cooling curve may be important. The cooling curve used here is a simplification and similarly the heating is approximated from UV heating of grains in the local solar neighborhood Gerritsen and Icke (1997) where there may be other significant contributions to the radiation field which may heat gas in the outer galactic disk, and this may vary spatially.

One may ask, after considering the results of this §3.1, §3.2 and §3.3, why the simulations of Wada and Norman (2007) show so much apparent activity in forming structures and driving turbulence? Some insight into this can be found by comparing their initial conditions to the ones used here. Their initial disk has density in the mid-plane of 3.4×10^{-22} to 3.4×10^{-21} g cm^{-2} which leads to rapid thermal instability. Figure (3.3) shows the maximum density of each isothermal initial condition used in this work, and the initial conditions of Wada and Norman (2007). The initial conditions of Wada and Norman (2007) can be seen to be far to the dense, unstable regime in figure (3.3). This guarantees that initially each local region of the disk will be strongly thermally unstable, encouraging its rapid fragmentation, both by thermal and gravitational instability.

Whereas Wada and Norman (2007) found their models drive quickly to a gravitoturbulent quasi-steady state, the results in §3.2 approach a state where all the gas is cool. The ultimate upper limit on the cool mass apprears to be only numerical. This suggests that if the quasi-steady state of self-gravitational and thermal instability driven turbulence found in Wada and Norman (2007) is indeed real, then it is a *necessarily global* phenomena. This is at odds with the purely *local* estimates discussed in §1.1.6 for the viability of this mechanism as a driving source for turbulence in galaxies. There are at least two ways this

might be resolved. First, a careful analysis of the stresses and mass fraction evolution in Wada and Norman (2007) type simulations should reveal if the state found is quasi-steady. Importantly, it should be shown that the cool mass fraction reaches a maximum, implying that as much gas is being heated by the turbulence as is cooling. Secondly, it may be that the multiphase nature of the disk invalidates the estimate of §1.1.6. As discussed there, the supply and dissipation parts of that estimate are based upon scalings which hold for isothermal gas. It was found that the estimate of §1.1.6 depended strongly on the length scales involved. Computations of these lengths may not by valid in a strongly two-phase medium.

If the velocity dispersion is to be driven by a local self-gravitational mechanism, the simulations suggest that the cool phase must exist everywhere in the disk where the velocity dispersion is seen. However, as the surface density of the disk drops, it will be increasingly difficult to achieve the critical pressure for the existence of the cool phase at the disk mid-plane. Detailed observation, extending the cool phase observations of de Blok and Walter (2006) might settle this by directly detecting a cool phase in low surface density extended galactic disks.

Similarly to the findings of Pinotek and Ostriker (2007), the simulations in this thesis suggest that the highest turbulent velocity dispersions are achieved in a disk with a cool phase. However, Pinotek and Ostriker (2007) were discussing magnetohydrodynamic turbulence in a stratified disk. They suggest that to achieve values less than ≈ 8 km s^{-1} for the observed combined thermal and turbulent velocity dispersion it is necessary for cool clouds to exist in the disk. This cool cloud condition is the same as is required for the more active regime of self-gravitational stress in the disk. It would therefore be

interesting to compute models similar to those seen here, but including magnetohydrodynamics so that the magnetic angular momentum transporting stress can be compared to the local self gravitational stress.

The results of this thesis suggest that there is a significant difference between the local angular momentum transport properties of a single phase galactic disk and of a two-phase galactic disk. Thus, it may be important to examine what importance local transfer of angular momentum can have on the formation and evolution of a disk galaxy. Currently, many approximations used in cosmological simulations of galaxy formation attempt to capture the multiphase gas dynamics as a subgrid model and do not fully include this two-phase nature. In particular some relevant approximations are: to use an isothermal gas, to enforce a minimum temperature on the order of 10^4 K, or to introduce multiple phases in each resolution element assuming a pressure equilibrium, without resolving the differing dynamics of each phase (see the review by Bryan, 2007). The central problem of all these approximations is that they attempt to capture the disk dynamics without resolving sufficiently small mass elements to track the dynamics of cool clouds.

Finally, a picture of the phase structure and dynamic structure of the outer regions of a galactic disk can be drawn. Three regimes, as shown in figure (3.24), can be identified, with the divisions between them drawn by the cutoff in star formation and the gas single-phase to two-phase transition:

I A region of single phase gas, closely following the heating-cooling equilibrium curve on the phase diagram, with $Q > 1$, and with pressure low enough to not support a two-phase medium, includes small perturbations

II A region where pressure is sufficient for cool clouds to form from existing

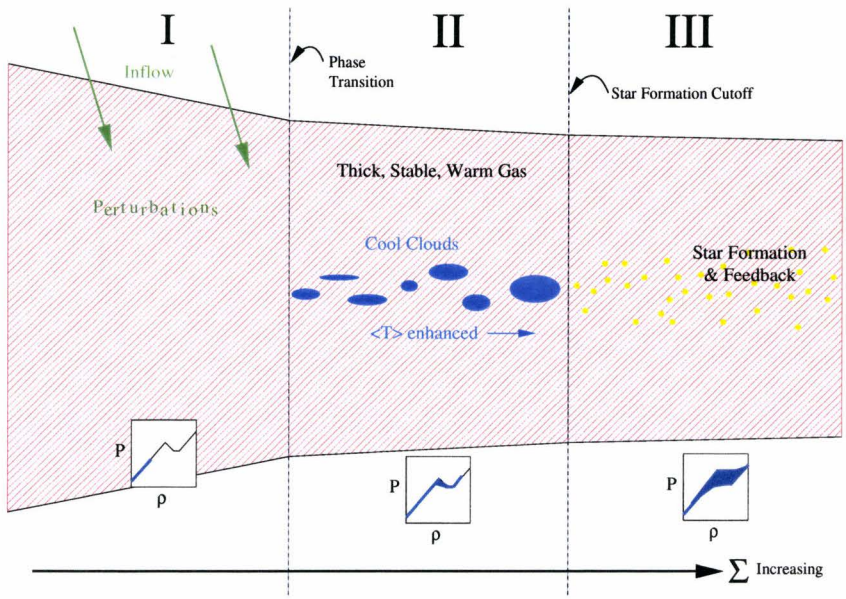

Figure 3.24: Three regimes of a galactic disk

small perturbations, forming a two-phase medium, enhanced angular momentum transporting stresses result

III The stellar disk, where the conditions for star formation are widely satisfied, and feedback (supernovae and outflows) drive turbulence.

Regions I and II are simple to form - thick warm gas disks are relatively physically simple, and the stellar disk is well known to exist. There are already a number of understood elements pointing to the nature of region II. Pinotek and Ostriker (2007) point out that the Schaye (2004) hypothesis, that the formation of the cool phase necessarily implies star formation, fails based on current observations showing that the phase change can occur outside of the limit of star formation. In the same work, they also find that magnetohydrodynamic effects in a region with cool clouds, such as in region II, may suppress star formation. The presence of star formation sets the division between re-

gions II and III. This cutoff may not be sharp, as discussed in §1.0.2, and it could be expected that locally star formation may happen in the cool phase of region II. The presence of stars, and their feedback (particularly supernovae, see Mac Low and Klessen (2004)) changes the dynamics and phase structure of gas from II to III. Between regions I and II the dividing line is drawn on the existence of the cool phase. Based on the results shown in this thesis, it can be said that in terms of local self-gravity there is an important dynamical divide between I and II.

Chapter 4

Conclusions

A new adaptive mesh shearing box implementation has been based on the FLASH code. It includes gasdynamics, a correction for numerical diffusion effects, self-gravity and cooling. Within this framework, a method for simulating local patches of a galactic gas disk, in three dimensions, has been developed. No gravitoturbulent quasi-steady state was found in a $Q = 1.16$ isothermal disk, indicating that local self-gravity driven turbulence might not be sustained in general in isothermal disks. The local approximation means this is a different phenomena than large scale spiral patterns in disks with similar Q. The lack of activity in this isothermal disks case does provide a starting point for investigating more complicated cases, specifically those involving a approximate cooling operator. In simulations with cooling, fixed mass and an isothermal initial condition it was found that the combination of mass and initial temperature fell either in a region where a single phase was formed, or where a two-phase medium was formed. While it was found that a disk with cooling and supporting only a single-phase medium did not develop significant angular momentum transporting self-gravitational stresses, disks with conditions such that a two-phase medium developed showed a vastly greater stress. Further, a disk model continuously accreting mass showed lo-

cal self-gravitational angular momentum transporting stresses increasing by four orders of magnitude upon the onset of thermal and gravitational instabilities and the formation of a two-phase medium. Finally, it has been observed that the dynamical change in the transport of angular momentum though self-gravity, and hence mass, following from the phase change and onset of a two-phase medium may mean that two significantly different regimes exist in an extended galactic disk, beyond the limit of star formation.

There are a number of areas where this work could be improved or built upon. As seen in §3.2 the physical scale at which filaments and cool clouds have formed in the simulations in this work has been strongly dependent on the grid resolution. It would be useful to increase the resolution at which these simulations have been run and to take numerical measures to limit the Field length to ensure that the process of collapse and fragmentation is properly resolved. One of the primary obstacles to achieving these larger, longer runs is the short cooling time when higher densities develop and the tendency of the FLASH Riemann solver to fail to converge if the short cooling time is ignored. Thus, a numerical gasdynamics method which more tightly couples cooling into the solution would be useful, as the cooling operator could then be integrated fully implicitly. A different gasdynamics method might also be able to alleviate the difficulty with gravity-gasdynamics coupling discussed in §2.4.3. The cooling operator used in this work, though consistent with related earlier work is a gross simplification. Most importantly, the heating component is adapted from observations of the galactic environment around the sun and may not be properly representative of condition in an extended galactic disk. This issue is most important in the high-density regime, the regime where it may impede star formation, as if in models of the type discussed in

this work the conditions for star formation are met, the model is then much less meaningful as a representation of the galactic disk past the limit of star formation or in the region of very low star formation rate. Though this work has only dealt with the gravitational and gasdynamic consequences of the formation of a two-phase medium, there should also be magnetohydrodynamic consequences in this context. These should be similar to the situation explored in the outer galaxy model of Pinotek and Ostriker (2007). A model like run A1 but including magnetic fields would be able to provide insight into the relative importance of gravitational and magnetohydrodynamics effects. As the criteria for star formation may not produce a clean edge at the limit of star formation, a model including an appropriate sub-grid model of star formation is still of interest, as this could contribute to the evolution of the phases significantly once the cool phase forms. Specifically, star formation should eventually transform the medium into a much more complicated multiphase situation and drive turbulence though mechanisms not directly tied to angular momentum transport. Hence, the transition point or region where the star formation rate significantly changes the dynamics of the gas would be particularly interesting to determine.

In the future, there are useful strategies to pursue in understanding the issues examined in this thesis, both numerically and observationally. Numerically, fully global simulations, extending at least as far as the accretion shock around the galaxy, and including an accurate treatment of the stellar component, heating, cooling, thermal conduction and magnetic fields, run with sufficient resolution to resolve the Jeans and Field lengths in the extended disk could be analyzed locally, allowing a more consistent analysis of the driving mechanisms behind turbulence in the extended galactic disc. Observationally,

further and definitive detection and mapping of the extent to which cool gas clouds exist in the extended disk of other galaxies would make significant contribution to the understanding of the extended galactic disk, as the existence of this structure should significantly affect the ability of the disk to sustain turbulent motions.

Bibliography

Abramowitz, M. and Stegun, I. A.: 1964, *Handbook of Mathematical Functions with Formulas, Graphs, and Mathematical Tables*, Dover, New York

Balbus, S. A. and Papaloizou, J. C. B.: 1999, ApJ **521**, 650

Begelman, M. C. and McKee, C. F.: 1990, ApJ **358**, 375

Binney, J. and Tremaine, S.: 1987, *Galactic dynamics*, Princeton, NJ, Princeton University Press, 1987, 747 p.

Brandenburg, A., Korpi, M. J., and Mee, A. J.: 2007, ApJ **654**, 945

Bryan, G. L.: 2007, in *EAS Publications Series*, Vol. 24 of *EAS Publications Series*, pp 77–88, doi: 10.1051/eas:2007060

Colella, P. and Woodward, P. R.: 1984, *Journal of Computational Physics* **54**, 174

de Blok, W. J. G. and Walter, F.: 2006, AJ **131**, 363

Debattista, V. P., Mayer, L., Carollo, C. M., Moore, B., Wadsley, J., and Quinn, T.: 2006, ApJ **645**, 209

Dib, S., Bell, E., and Burkert, A.: 2006, ApJ **638**, 797

Dickey, J. M., Hanson, M. M., and Helou, G.: 1990, ApJ **352**, 522

Elmegreen, B. G. and Hunter, D. A.: 2006, ApJ **636**, 712

Elmegreen, B. G. and Parravano, A.: 1994, ApJ **435**, L121+

Field, G. B.: 1965, ApJ **142**, 531

Freeman, K. and Bland-Hawthorn, J.: 2002, ARA&A **40**, 487

Fromang, S. and Papaloizou, J.: 2006, A&A **452**, 751

Fryxell, B., Olson, K., Ricker, P., Timmes, F. X., Zingale, M., Lamb, D. Q., MacNeice, P., Rosner, R., Truran, J. W., and Tufo, H.: 2000, ApJS **131**, 273

Gammie, C. F.: 2001, ApJ **553**, 174

Gazol, A., Vázquez-Semadeni, E., and Kim, J.: 2005, ApJ **630**, 911

Gerritsen, J. P. E. and Icke, V.: 1997, A&A **325**, 972

Goldreich, P. and Lynden-Bell, D.: 1965a, MNRAS **130**, 97

Goldreich, P. and Lynden-Bell, D.: 1965b, MNRAS **130**, 125

Hawley, J. F., Gammie, C. F., and Balbus, S. A.: 1995, ApJ **440**, 742

Hill, G.: 1878, *Amer. J. Math* **1**, 5

Johnson, B. M. and Gammie, C. F.: 2003, ApJ **597**, 131

Johnson, B. M. and Gammie, C. F.: 2005a, ApJ **626**, 978

Johnson, B. M. and Gammie, C. F.: 2005b, ApJ **635**, 149

Kennicutt, Jr., R. C.: 1989, ApJ **344**, 685

Kim, W.-T. and Ostriker, E. C.: 2007, ApJ **660**, 1232

Koyama, H. and Inutsuka, S.-i.: 2004, ApJ **602**, L25

Kritsuk, A. G. and Norman, M. L.: 2002, ApJ **569**, L127

Levine, E. S., Blitz, L., and Heiles, C.: 2006a, *Science* **312**, 1773

Levine, E. S., Blitz, L., and Heiles, C.: 2006b, ApJ **643**, 881

Lynden-Bell, D. and Kalnajs, A. J.: 1972, MNRAS **157**, 1

Mac Low, M.-M. and Klessen, R. S.: 2004, *Reviews of Modern Physics* **76**, 125

Masset, F.: 2000, A&AS **141**, 165

Parker, E. N.: 1953, ApJ **117**, 431

Piontek, R. A. and Ostriker, E. C.: 2007, *ArXiv Astrophysics e-prints*

Pohlen, M., Erwin, P., Trujillo, I., and Beckman, J. E.: 2007, *ArXiv e-prints*

706

Sánchez-Salcedo, F. J., Vázquez-Semadeni, E., and Gazol, A.: 2002, ApJ **577**, 768

Santillan, A., Sanchez-Salcedo, F. J., and Franco, J.: 2007, *ArXiv e-prints* 705

Schaye, J.: 2004, ApJ **609**, 667

Sellwood, J. A. and Balbus, S. A.: 1999, ApJ **511**, 660

Shen, Y., Stone, J. M., and Gardiner, T. A.: 2006, ApJ **653**, 513

Strang, G.: 1968, *SIAM J. Numer. Anal.* **5**, 506

Tasker, E. J. and Bryan, G. L.: 2006, ApJ **641**, 878

Toomre, A.: 1964, ApJ **139**, 1217

Truelove, J. K., Klein, R. I., McKee, C. F., Holliman, II, J. H., Howell, L. H., and Greenough, J. A.: 1997, ApJ **489**, L179+

Wada, K., Meurer, G., and Norman, C. A.: 2002, ApJ **577**, 197

Wada, K. and Norman, C. A.: 1999, ApJ **516**, L13

Wada, K. and Norman, C. A.: 2001, ApJ **547**, 172

Wada, K. and Norman, C. A.: 2007, ApJ **660**, 276

Warren, B. E., Jerjen, H., and Koribalski, B. S.: 2004, AJ **128**, 1152

Wisdom, J. and Tremaine, S.: 1988, AJ **95**, 925

Zingale, M., Dursi, L. J., ZuHone, J., Calder, A. C., Fryxell, B., Plewa, T., Truran, J. W., Caceres, A., Olson, K., Ricker, P. M., Riley, K., Rosner, R., Siegel, A., Timmes, F. X., and Vladimirova, N.: 2002, ApJS **143**, 539